

A spectral atlas of post-main-sequence stars in ω Centauri: kinematics, evolution, enrichment and interstellar medium

Jacco Th. van Loon^{1*}, Floor van Leeuwen², Barry Smalley¹, Andrew W. Smith¹, Nicola A. Lyons¹, Iain McDonald¹, Martha L. Boyer³

¹*Astrophysics Group, Lennard-Jones Laboratories, Keele University, Staffordshire ST5 5BG, United Kingdom*

²*Institute of Astronomy, Madingley Road, Cambridge CB3 0HA, United Kingdom*

³*Department of Astronomy, 116 Church Street SE, University of Minnesota, Minneapolis, MN 55455, USA*

Submitted July 2007

ABSTRACT

We present a spectral atlas of the post-main-sequence population of the most massive Galactic globular cluster, ω Centauri. Spectra were obtained of more than 1500 stars selected as uniformly as possible from across the (B, B–V) colour-magnitude diagram of the proper motion cluster member candidates of van Leeuwen et al. (2000). The spectra were obtained with the 2dF multi-fibre spectrograph at the Anglo Australian Telescope, and cover the approximate range $\lambda \sim 3840\text{--}4940 \text{ \AA}$ at a resolving power of $\lambda/\Delta\lambda \simeq 2000$. This constitutes the most comprehensible spectroscopic survey of a globular cluster. We measure the radial velocities, effective temperatures, metallicities and surface gravities by fitting ATLAS9 stellar atmosphere models. We analyse the cluster membership and stellar kinematics, interstellar absorption in the Ca II K line at 3933 \AA , the RR Lyrae instability strip and the extreme horizontal branch, the metallicity spread and bimodal CN abundance distribution of red giants, nitrogen and s-process enrichment, carbon stars, pulsation-induced Balmer line emission on the asymptotic giant branch (AGB), and the nature of the post-AGB and UV-bright stars. Membership is confirmed for the vast majority of stars, and the radial velocities clearly show the rotation of the cluster core. We identify long-period RR Lyrae-type variables with low gravity, and low-amplitude variables coinciding with warm RR Lyrae stars. A barium enhancement in the coolest red giants indicates that 3rd dredge-up operates in AGB stars in ω Cen. This is distinguished from the pre-enrichment by more massive AGB stars, which is also seen in our data. The properties of the AGB, post-AGB and UV-bright stars suggest that RGB mass loss may be less efficient at very low metallicity, $[\text{Fe}/\text{H}] \ll -1$, increasing the importance of mass loss on the AGB. The catalogue and spectra are made available via CDS.

Key words: stars: AGB and post-AGB – stars: carbon – stars: horizontal branch – stars: kinematics – stars: oscillations – globular clusters: individual: ω Cen/NGC 5139

1 INTRODUCTION

The most massive Galactic globular cluster, ω Centauri (NGC 5139) is of considerable interest both for astrophysics and cosmology. Being the most populous star cluster in our galaxy, one has a chance to catch stars in their most rapid phases of post-main-sequence evolution, such as post-Asymptotic Giant Branch (post-AGB) stars which evolve on timescales of 10^5 years or less to become white dwarfs after significant mass return into the interstellar medium (ISM). Its proximity, $d \sim 5 \text{ kpc}$ (e.g., Del Principe et al. 2006; van

de Ven et al. 2006; Caputo et al. 2002), and relatively low foreground extinction, $E(B - V) \sim 0.11 \text{ mag}$ (Lub 2002), further aid in detailed studies of its constituents. Besides, ω Cen may hold vital clues to understanding the assembly of massive galaxies and the fate of the many satellites predicted to have formed in the Λ -CDM cosmological paradigm (Klypin et al. 1999). Understanding its dynamical history and possible origin within a larger galactic body are key to understanding the nature of ultra-massive globular clusters such as G 1 in the Local Group spiral galaxy M 31 (e.g., Gebhardt et al. 2002), the ultra-compact dwarf galaxies found in the Fornax cluster (Drinkwater et al. 2004), and the tidal

* E-mail: jacco@astro.keele.ac.uk

dissolution of stellar systems that then populate the Galactic halo with field stars.

It has long been known that ω Centauri hosts stars spanning a range of metallicities, contrary to the paradigm that globular clusters are co-eval, chemically uniform systems. Norris et al. (1996) determined calcium abundances of bright Red Giant Branch (RGB) stars and found that about 80 per cent belong to a metal-poor component now identified with a metallicity $[\text{Fe}/\text{H}] \simeq -1.7$, with the remaining 20 per cent constituting a metal-richer component, of $[\text{Fe}/\text{H}] \simeq -1.2$. Lee et al. (1999) and Pancino et al. (2000, 2002), using optical colour-magnitude diagrams, discovered a third sub-population in the form of an anomalous feature in the RGB morphology, the RGB-a; these red giants are, with $[\text{Fe}/\text{H}] \simeq -0.6$, an order of magnitude more metallic than the main population of ω Cen.

Lee et al. (1999) proposed an extended period of star formation, lasting ~ 2 Gyr, to explain the different populations through a chemical enrichment scenario within a larger, now-disrupted system, a scenario proposed previously also by Zinnecker et al. (1988) and Freeman (1993). Although Stanford et al. (2006a) do indeed find that the metal-rich stars are the youngest by 2-4 Gyr, Sollima et al. (2005) find that the metal-rich and intermediate-metallicity populations must have formed within 2 Gyr from the oldest metal-poor stars. The situation may be more complicated: Villanova et al. (2007) suggest that the metal-rich stars and a third of the metal-poor stars are the *oldest*, with the remaining two-thirds of metal-poor stars and the intermediate-metallicity stars being younger by 3-4 Gyr.

A double main sequence was discovered by Anderson (1997; see also Bedin et al. 2004), and interpreted by Norris (2004) in terms of the three RGB sub-populations; counter-intuitively, the *less* metal-poor population must correspond to the *bluer* main sequence (confirmed spectroscopically by Piotto et al. 2005). Norris explained this by the intermediate-metallicity population being enhanced in helium. Though reconciling the observations, the helium enhancement poses a challenge for chemical evolution models, as neither all of the cluster sub-giant stars nor all the intermediate-metallicity RR Lyrae variables on the Horizontal Branch (HB) are helium-rich (Villanova et al. 2007; Sollima et al. 2006).

The mixed stellar populations complicate studies of stellar evolution in ω Cen, but on the other hand it offers the possibility to compare the evolution of stars between these different populations. Questions that remain to be answered include the mechanism of mass loss on the RGB, how (and why) it varies between different stars, and how this is reflected in the properties of the HB (see Catelan 2005 for a review), in particular the extreme HB (D’Cruz et al. 1996). A type of HB star, RR Lyrae-type pulsators are distance indicators. The RR Lyrae-derived distance to ω Cen ($d = 5.5 \pm 0.04$ kpc: Del Principe et al. 2006) differs from that derived from the internal kinematics ($d = 4.8 \pm 0.3$ kpc: van de Ven et al. 2006), and it is therefore important to reach a full understanding of the RR Lyrae phenomenon. Different types of RR Lyrae exist in ω Cen, pulsating in different modes, and stars are found with colours and magnitudes that overlap with those of RR Lyrae but which are not strong pulsators (Sandage & Katem 1968). It is not clear to what extent this is due to different evolutionary stages,

differences in RGB mass loss, or a result of the spread in elemental abundances.

During the subsequent AGB and post-AGB evolution additional mass is returned to the ISM, possibly enriched in s-process elements and/or dust grains. It is not clear, though, how many globular cluster stars reach the AGB, how many of those experience 3rd dredge-up, and whether globular cluster carbon stars must all have formed through external pollution. It is also not understood how AGB mass loss and dust formation proceeds at a considerably sub-solar metallicity (van Loon 2006). A different question altogether is how much post-AGB stars contribute to the UV light from old stellar systems such as elliptical galaxies; this depends on the zero-age post-AGB luminosity function and the timescale of post-AGB evolution.

The present study was motivated by the van Leeuwen et al. (2000) survey, who determined the proper motion membership probabilities of nearly 10,000 stars within half a degree from the centre of the cluster down to a photographic magnitude of ~ 16.5 . We obtained medium-resolution follow-up spectroscopy in the B-band of more than 1500 probable members. Whilst other follow-up studies concentrated on obtaining radial velocities to map the 3-dimensional kinematical structure of the cluster (Reijns et al. 2006) our survey covers sufficient line diagnostics to be able to also automatically determine temperatures, gravities and metallicities through fitting of the synthetic spectra of model atmospheres. This allows us to break the degeneracies encountered in colour-magnitude diagrams, and to study the effect of metallicity on stellar evolution. Abundances of carbon, nitrogen and s-process elements such as barium can be compared to assess the degree of enrichment from internal nucleosynthesis and external pollution. The survey also provides candidates for more detailed follow-up studies, including the use of blue-HB stars as torches shining through the intervening ISM. Preliminary results were presented in van Loon (2002), and the spectra are currently used to support our *Spitzer Space Telescope* IRAC+MIPS atlas of the cluster (Boyer et al. 2007; McDonald et al., in preparation). The remainder of this paper is organised as follows:

2 Spectroscopy with the AAT/2dF

2.1 Observations

2.2 Data reduction

3 The target sample

4 The database

4.1 The measurement of stellar parameters

4.2 Data quality and reliability of the model fits

4.3 Description of the electronic database

5 Results

5.1 Cluster membership and internal kinematics

5.2 Interstellar absorption by ionised gas

5.3 Metallicity and the morphology of the Hertzsprung-Russell Diagram

5.4 The first ascent Red Giant Branch (RGB)

5.4.1 The nature of the anomalous RGB branch

5.4.2 Nitrogen enrichment

5.4.3 Chromospheric activity

5.5 The RR Lyrae instability strip

5.6 Extreme Horizontal Branch stars (EHB)

5.7 The Asymptotic Giant Branch (AGB)

- 5.7.1 M-type stars
- 5.7.2 Pulsation
- 5.7.3 Dredge-up
- 5.8 Carbon stars
- 5.9 Post-AGB and UV-bright stars
- 6 Discussion
 - 6.1 Late stages of evolution of metal-poor stars
 - 6.1.1 Horizontal Branch stars and RR Lyrae variables
 - 6.1.2 Asymptotic Giant Branch stars and dredge-up
 - 6.1.3 Mass loss and post-giant branch evolution
 - 6.2 Cluster formation and evolution
 - 6.2.1 The nature of the multiple stellar populations
 - 6.2.1 Gas retention and accretion
- 7 Summary of conclusions

2 SPECTROSCOPY WITH THE AAT/2DF

2.1 Observations

The 2-degree Field (2dF) multi-fibre spectrograph at the Anglo Australian Telescope (AAT) was used on the second half of the nights on 26 and 27 February and 1 and 2 March, 2000, in combination with the 1200B grating to obtain spectra in the approximate range $\lambda \sim 3840\text{--}4940 \text{ \AA}$ at a resolving power of $\lambda/\Delta\lambda \simeq 2000$. A log of the observations is presented in Table 1.

Each of the 400 fibres has a diameter of $2''$ projected on the sky, limiting spectroscopy in crowded stellar fields. The proximity of ω Cen, the fact that it has a relatively low stellar density, and a careful selection procedure (Section 3) enables us to obtain uncontaminated spectra of the majority of post-main-sequence stars in this cluster. Despite its large angular size, ω Cen does not fill the full 2° field, and fibre allocation was therefore limited by the physical size of the fibre buttons and crossings of the fibre arms. The field was acquired using four fiducial stars. These were selected from stars with a high cluster membership probability (Section 3) to safeguard the relative astrometry of the targets. Subsequent fields were observed using alternating fibre-positioning plates.

Because spectra are displayed adjacently on each of two Charge Coupled Devices (CCDs), bright targets defined as having B-band magnitudes $B < 13.5$ mag were observed separately from fainter targets. The bright targets received three exposures of 5 minutes each, whilst the individual exposures of the fainter targets were normally 25 minutes in duration. Typically, in each observation ~ 200 fibres were used to obtain spectra of the sky; these positions were distributed on a grid with a density declining with distance from the centre, and they were checked for the absence of contaminating stellar light.

Zero-integration CCD readouts (“bias” frames) were taken to measure the electronic offset and readout noise properties, and long integrations with the shutter closed were taken to measure the dark current. Exposures of an Fe/Ar arc lamp spectrum were taken for wavelength calibration, at each telescope pointing to alleviate the effects of flexure within the instrument. Exposures of a quartz “white-light” lamp were also obtained, through the fibres at each telescope pointing, to measure the pixel-to-pixel variations in the response of the CCD. For each observation, three

exposures of 5 minutes each were obtained at a position off-set from the target field by 0.5° , to measure the relative throughput of the fibres.

The observing conditions were typical, with the seeing varying between 1.2 and $2.5''$, and some scattered clouds on the February nights. The overall quality of the spectra was excellent, and the analysis was almost never limited by the signal-to-noise (S/N) ratio even for the faintest targets ($B \sim 16.5$ mag). S/N ratios computed from pixel-to-pixel variations between repeat observations are typically ~ 50 per pixel around $B = 16$ mag to >100 per pixel for $B < 15$ mag in the redder half of the spectrum, and ~ 30 in the bluer half of the spectrum. The S/N ratio per spectral resolution element is roughly a factor $\sqrt{2}$ higher than this.

2.2 Data reduction

The data were reduced using version 2.3 (June 2002) of 2dFdr. The positions of the (curved) spectra on the CCD are parameterised in a default tram map, which was fitted to the data by applying rotation and translation corrections. The fits and fibre identifications were checked manually, updating the table with broken fibres where necessary.

First the fibre flatfield and arc exposures were reduced. Then the off-set sky frames were reduced, which included subtracting scattered light and combination of the individual frames via their median (on a pixel-to-pixel basis). The target fields were divided through by the flatfield, and scattered light was subtracted. The spectra were extracted from the frames by fitting the profile perpendicular to the direction of dispersion with a gaussian, rejecting anomalous pixel values if they deviated by more than $20\times$ the noise level. The multiple exposures of the same star on a given night were combined via their mean, after adjusting the continuum levels (applying a smoothing of 101 pixels) and rejecting pixel values that deviated by more than five times the noise level.

Due in part to contaminating light in the off-set sky observations, the fibre throughputs were ill-determined. This resulted in large errors in the sky subtraction, in particular for the faintest targets. We therefore performed a second-order sky subtraction: for each wavelength, up to 5 sky values at either side (on the CCD) of the object fibre were averaged, excluding the highest and lowest values. This also improved the correction for scattered light on the CCD.

3 THE TARGET SAMPLE

The basis for the spectroscopic target sample was the proper motion survey by van Leeuwen et al. (2000), which comprises 9847 stars, and we shall refer to their catalogue numbers for star identifications (Leiden Identifier, or LEID). Stars were selected for possible spectroscopic observation if they had a cluster membership probability of at least 90 per cent (but see below for variable stars), and both B and V-band photometry. A further 172 stars were rejected because of neighbouring stars within $2''$ that could contaminate the light within the fibre.

Next, a grid was overlaid on the (B, B–V) diagram, with a grid spacing of $\Delta B = 0.1$ and $\Delta(B - V) = 0.05$. In each pass, the star within a grid element that had the (next) largest distance from the cluster centre was assigned

Table 1. Log of observations, with date and airmass given for the middle of the exposures. The value for the seeing is only an indicative figure for the conditions at the time of observation. The mean velocity, $\langle v_{\text{LSR}} \rangle$ was computed relative to the Local Standard of Rest (LSR) along with the standard deviation, for the N_{cluster} probable cluster members — i.e. excluding N_{field} obvious foreground stars.

| ID | UT date | airmass | seeing | plate | CCD | t_{exp} (s) | N_{cluster} | N_{field} | N_{sky} | selection | $\langle v_{\text{LSR}} \rangle$ |
|----|---------------|---------|--------|-------|-----|----------------------|----------------------|--------------------|------------------|---------------|----------------------------------|
| 1a | 2000 02 26.72 | 1.04 | 1.3'' | 1 | 1 | 4 × 300 | 41 | 1 | 120 | $B < 13.5$ | 234 ± 16 |
| 1b | ... | ... | ... | ... | 2 | ... | 44 | - | 116 | ... | 232 ± 14 |
| 2a | 2000 02 26.79 | 1.11 | 1.7'' | 0 | 1 | 3 × 300 | 14 | 1 | 143 | ... | 243 ± 13 |
| 2b | ... | ... | ... | ... | 2 | ... | 33 | - | 131 | ... | 232 ± 13 |
| 3a | 2000 02 27.64 | 1.11 | 2.0'' | 0 | 1 | 3 × 1200 | 134 | 5 | 31 | $B \geq 13.5$ | 247 ± 15 |
| 3b | ... | ... | ... | ... | 2 | ... | 124 | 2 | 36 | ... | 227 ± 14 |
| 4a | 2000 02 27.73 | 1.04 | 2.0'' | 1 | 1 | 3 × 1500 | 126 | 3 | 35 | ... | 241 ± 18 |
| 4b | ... | ... | ... | ... | 2 | ... | 126 | 4 | 38 | ... | 232 ± 14 |
| 5a | 2000 03 01.55 | 1.43 | 1.5'' | 1 | 1 | 3 × 1500 | 121 | 1 | 47 | ... | 246 ± 15 |
| 5b | ... | ... | ... | ... | 2 | ... | 128 | - | 28 | ... | 238 ± 14 |
| 6a | 2000 03 01.64 | 1.11 | 1.2'' | 0 | 1 | 3 × 1500 | 111 | 1 | 41 | ... | 244 ± 14 |
| 6b | ... | ... | ... | ... | 2 | ... | 117 | 1 | 47 | ... | 240 ± 12 |
| 7a | 2000 03 01.74 | 1.06 | 2.2'' | 1 | 1 | 3 × 1500 | 109 | - | 48 | ... | 240 ± 17 |
| 7b | ... | ... | ... | ... | 2 | ... | 103 | - | 43 | ... | 234 ± 11 |
| 8a | 2000 03 02.64 | 1.10 | 1.4'' | 0 | 1 | 3 × 1500 | 100 | 1 | 53 | ... | 243 ± 16 |
| 8b | ... | ... | ... | ... | 2 | ... | 105 | 2 | 47 | ... | 232 ± 11 |
| 9a | 2000 03 02.73 | 1.05 | 2.5'' | 1 | 1 | 4 × 1500 | 88 | 4 | 72 | ... | 246 ± 16 |
| 9b | ... | ... | ... | ... | 2 | ... | 103 | 1 | 59 | ... | 235 ± 11 |

the (next) highest priority. This alleviates the natural bias towards the most populous parts of the cluster and colour-magnitude diagram. As a result, our spectral atlas samples not only the central parts of the cluster and the “spine” of the RGB and HB, but includes the cluster fringes (which also makes fibre allocation easier) and rare objects in trace populations or brief phases of evolution. In seven such passes, 2477 stars were picked, of which 688 in the highest category. Of the remaining stars, 98 fiducial stars were selected with $B < 14$ mag (all of these have $(B - V) > 1$ mag) and no neighbours within 3''. This left 4681 stars to be available for fibre allocation at the lowest priority.

A further 15 stars were observed that did not satisfy the 90 per cent proper motion membership probability criterion, but which are of special interest. These comprise variable stars (mostly of RR Lyrae type) and the two brightest (in the B-band) suspected members: post-AGB star candidates #16018 (Fehrenbach’s star; ROA 24, Woolley 1966) and the long-period Cepheid variable #32029 (V1; $P = 32$ d). To ensure sufficient coverage of the RR Lyrae instability strip, the highest priority was assigned to all known RR Lyrae stars and “non-variable” stars within the RR Lyrae “box”, which we defined as $0.3 < (B - V) < 0.6$ and $14.5 < B < 15.2$. Other stars of special interest include the longest-period confirmed variable star member of ω Cen, #44262 (V42; $P = 149$ d), and two known carbon stars, #41071 (ROA 577) and #52030 (ROA 55). The long-period variable star #34041 ($P = 508$ d) was not observed, as its proper motion clearly places it outside of the cluster. In total, 1766 spectra were obtained, including 142 RR Lyrae and 238 duplicate observations of the same star.

The resulting distribution on the sky of the observed stars shows that all of the cluster is well sampled, from the outskirts into the core (Fig. 1). Similarly, the observations sample the colour-magnitude diagram very well (Fig. 2), with a greatly reduced bias towards the densest populated parts of the giant branches. They cover the colour spread

at the top of the RGB and AGB, the anomalous branch at $(B - V) > 1$ and $B \sim 15$, the extreme blue HB (which turns vertical in a (B, B-V) diagram), and several “UV-bright” stars above and to the blue of the HB.

4 THE DATABASE

4.1 The measurement of stellar parameters

Each 2dF spectrum was matched with a model spectrum in an automatic fashion. To this end, 2503 ATLAS9 model atmospheres (Kurucz 1993) were generated on a grid of stellar parameters, viz. effective temperature, T_{eff} , metallicity (scaled solar abundances), $[\text{Fe}/\text{H}]$, and surface effective gravity, $\log g_{\text{eff}}$ (Fig. 3). Synthetic spectra were computed for these models with SYNTH (Kurucz 1993), at the spectral resolving power of the 2dF spectra but sampling at a ten times higher rate to enable measurement of the radial velocity shift to a precision of a few km s^{-1} — even though the *accuracy* of this value is less (see Sect. 4.2). The spectra were interpolated to increase the grid resolution to steps of $\Delta[\text{Fe}/\text{H}]=0.25$.

The atomic line list used in the models is quite extensive and includes many (but not all) transitions in the CH, CN and TiO molecules (Kurucz 1999). Besides omissions such as the C_2 molecule which is seen in carbon stars (Sect. 5.8), some of the atomic data are uncertain (e.g., helium, Sect. 5.6) or the atmosphere model has difficulty reproducing the exact strength (as in the case of the molecules). Abundance anomalies are not uncommon in post-main-sequence stars as a result of surface enrichment with specific products of nucleosynthesis, most spectacularly seen in carbon stars, and ω Cen is known for the abundance anomalies seen even in its main-sequence stars (Stanford et al. 2006b, 2007). Nevertheless, these models produce useful stellar classifications for a global analysis of the cluster population and stellar

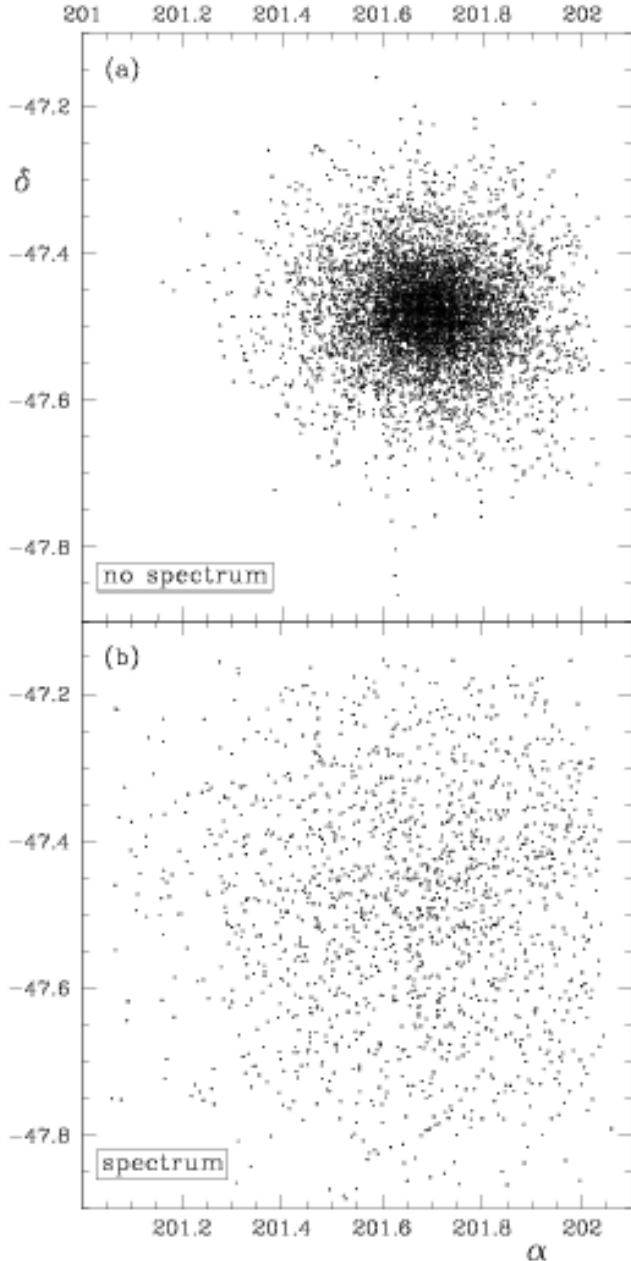


Figure 1. Distribution on the sky of (a) all the potential targets minus the observed stars and (b) the stars that were actually observed. There is very little bias towards the centre of the cluster, without avoiding it altogether, and the outskirts are especially well sampled.

evolution, and as a starting point for more detailed studies of individual (classes of) objects.

Expanding the observed spectrum, f , in each spectral point a as a Taylor series to second order,

$$f(x) \simeq f(a) + (x - a) \left. \frac{df}{dx} \right|_{x=a} + \frac{(x - a)^2}{2!} \left. \frac{d^2f}{dx^2} \right|_{x=a}, \quad (1)$$

and similarly for the model spectrum, g , we do not simply require that the spectra reach similar values in each point, $f(a) \simeq g(a)$, but that the *shape* of the spectra are similar in

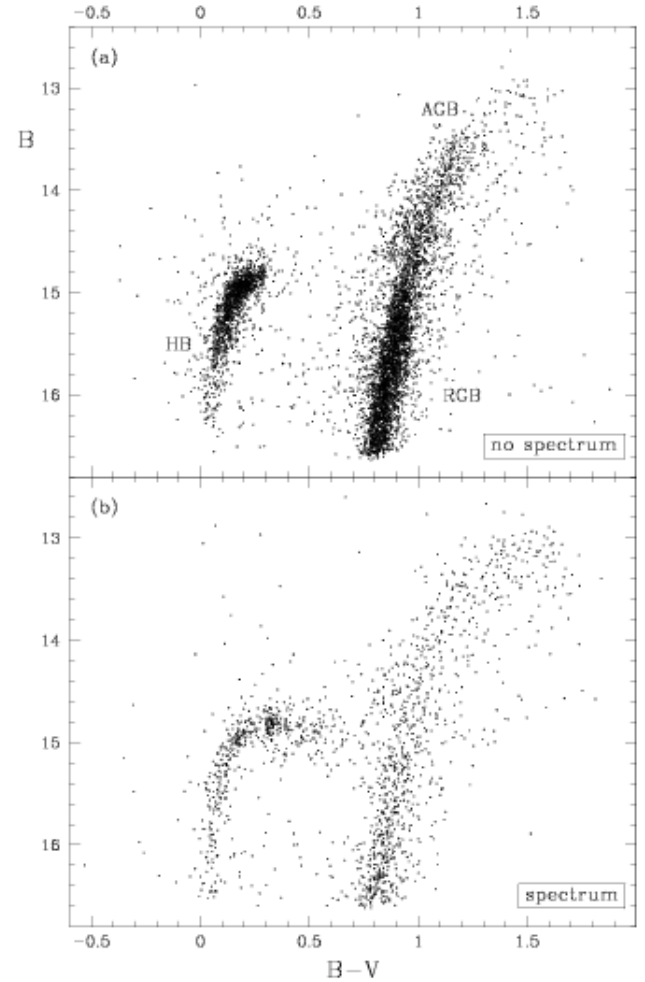


Figure 2. Distribution in the $(B, B-V)$ diagram of (a) all the potential targets minus the observed stars and (b) the stars that were actually observed. All regions in the diagram all sampled, with the only strong bias remaining being the RR Lyrae variables and non-variables with similar colours and magnitudes.

each point, $f(x) \simeq g(x)$. Thus, with N spectral points and $\Delta_a = f(a) - g(a)$, we minimise the statistic

$$\chi^2 = \sum_{i=1}^N \left(\frac{\Delta_{i+2} + \Delta_{i+1} - \Delta_{i-1} + \Delta_{i-2}}{2} \right)^2 \quad (2)$$

(see Appendix A). It tests for similarity in intensity, slope, and curvature at any given point in the spectrum. It measures correlated behaviour of the residuals and thus enhances the ability to detect and correctly reproduce weak spectral features, in contrast to the uncorrelated behaviour of noise or spectral mismatch.

Before evaluating χ^2 the observed spectrum is first normalised to the continuum in the model spectrum, using a running boxcar with a width of 100 pixels ($\sim 100 \text{ \AA}$). The result of this procedure is that the fitting is less sensitive to low-frequency structure in the spectrum, and thus less affected by uncertainties in the wavelength-dependent instrumental throughput or the exact level of the continuum. The latter is important in very cool stars, where the atomic and molecular absorption veils much of the continuum.

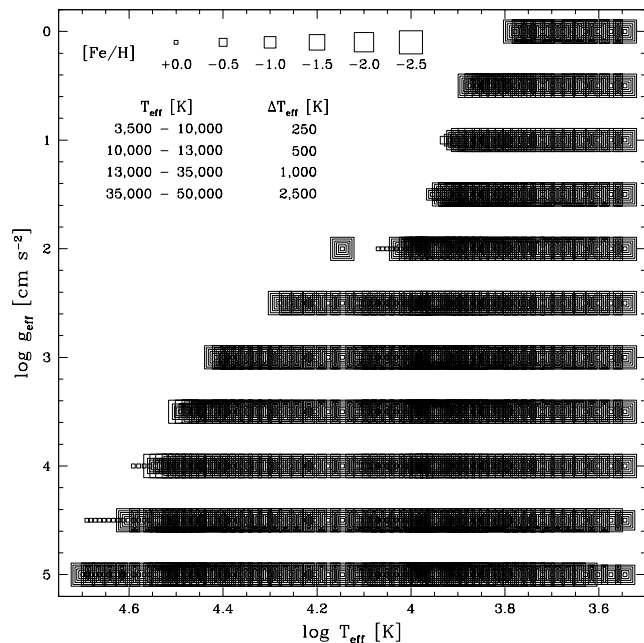


Figure 3. Grid of ATLAS9 model atmospheres that were generated and for which synthetic spectra were computed with SYNTHÉ. Spectra were interpolated to provide approximate spectra for metallicities of $[\text{Fe}/\text{H}] = -0.25, -0.75, -1.25, -1.75$ and -2.25 .

The procedure is repeated after applying a velocity offset to the model spectra using the non-relativistic Doppler formula. Initial offsets are between $\Delta v = -200$ and 400 km s^{-1} in steps of 100 km s^{-1} . Subsequently, these steps are diminished by a factor 5 and applied around the velocity at which χ^2 was thus far minimal, with a final velocity step of 1 km s^{-1} .

As a compromise between maximising multiplexity and maximising fidelity, the χ^2 was evaluated within $\lambda = 3910$ to 4940 \AA . Most spectra extend beyond that, but the data near the edges are generally of lower quality because of spectrum extraction and correction difficulties near the rims of the CCDs. Also, the diminished sensitivity of the CCDs at ultraviolet wavelengths below $\lambda \sim 3900 \text{ \AA}$ reduces the S/N ratio, a problem in particular for the red giants. Nevertheless, there are spectral features in the ultraviolet that remain useful to be compared with the model spectrum that best fits the rest of the observed spectrum, such as higher order lines of the hydrogen Balmer series in the hotter stars and a strong CN band in some of the cooler stars.

The $\text{H}\beta$, $\text{H}\gamma$ and $\text{H}\delta$ line profiles were checked for signs of possible emission: if the maximum difference between the observed spectrum and the best model spectrum was in excess of both 20 per cent of the continuum and three times the standard deviation determined outside of the line profiles, then the model fitting procedure was repeated excluding those points and the two points at either side of them. A flag was set to 1 in the catalogue. The same was done for the Ca H+K lines, which sometimes exhibit line emission arising from a chromosphere. If detected, the flag was set to 2 (or 3 if both the hydrogen and calcium lines showed signs of possible emission).

Bad data were removed; a spectrum was not considered if more than half of the data were rejected, in which case

Table 2. Average differences between repeat measurements.

| Selection | N | Δv (km s^{-1}) | $\frac{\Delta T}{\langle T \rangle}$ | $\Delta \log g$ (cm s^{-2}) | $\Delta [\text{Fe}/\text{H}]$ (dex) |
|-------------------------|-----|--------------------------------------|--------------------------------------|---|--|
| All | 235 | 11.1 | 0.06 | 0.90 | 0.40 |
| $B-V < 0.3$ | 40 | 13.4 | 0.13 | 0.77 | 0.62 |
| $0.3 \leq B-V \leq 0.6$ | 86 | 10.8 | 0.04 | 1.15 | 0.27 |
| $0.6 < B-V < 1$ | 82 | 10.8 | 0.05 | 0.85 | 0.47 |
| $B-V \geq 1$ | 27 | 9.1 | 0.04 | 0.43 | 0.31 |

the flag was set to 9. Including a few spectra that obviously had no signal to speak of, a total of only 12 spectra were rejected from the analysis, leaving 1754 classified spectra.

As an indication of, respectively, the total flux collected on the CCD and the recorded spectral slope, we define a magnitude and colour that we compute from the observed spectrum. The magnitude is broadly similar to the B-band, and is defined as

$$B' \equiv 25 - 2.5 \log \left(\sum_{i=1}^N f(i) \right), \quad (3)$$

while the colour is defined in relation to the blue and red halves within this band:

$$B_1 - B_2 \equiv -2.5 \log \left(\frac{\sum_{i=1}^{N/2} f(i)}{\sum_{j=N/2}^N f(j)} \right). \quad (4)$$

4.2 Data quality and reliability of the model fits

Several checks can be made to ascertain the quality of the observed spectra and the reliability of the model fits. In the following we will discuss the accuracy of the radial velocities, the level of variation between repeat observations, a comparison between the photometry and spectroscopic measurements, and a number of spectral oddities that are not well reproduced by the models.

The number statistics in Table 1 of the 1754 classified spectra includes a computation of the mean velocity per CCD per observation. Without exception, the mean velocity on CCD 1 is larger than on CCD 2: $\langle v_{\text{LSR}} \rangle_1 = 243 \pm 4 \text{ km s}^{-1}$ versus $\langle v_{\text{LSR}} \rangle_2 = 234 \pm 4 \text{ km s}^{-1}$, where the errors are standard deviations. Because this effect is larger than the variations between separate observations, we correct for it by lowering all radial velocities from CCD 1 by 4 km s^{-1} and by increasing all radial velocities from CCD 2 by an equal amount.

Of the 238 repeat observations, 235 pairs of spectra were classified. The average absolute values of the differences in the obtained parameters (Table 2) give us a rough estimate of the accuracy of these measurements, as the variance of two measurements is half the square of their difference (Bland & Altman 1996). The velocity is thus determined with an accuracy of $\sigma_v \sim 11/\sqrt{2} = 8 \text{ km s}^{-1}$; slightly worse for the bluest stars but better for the reddest — this is almost certainly due to the increased multiplexity of the cool star spectra. A similar effect is seen in the relative error on the temperature, where the temperature is generally determined with an accuracy of ~ 3 to 4 per cent except for the bluest stars ($B - V < 0.3$) where the temperature cannot be determined to better than 9 per cent. The accuracy of

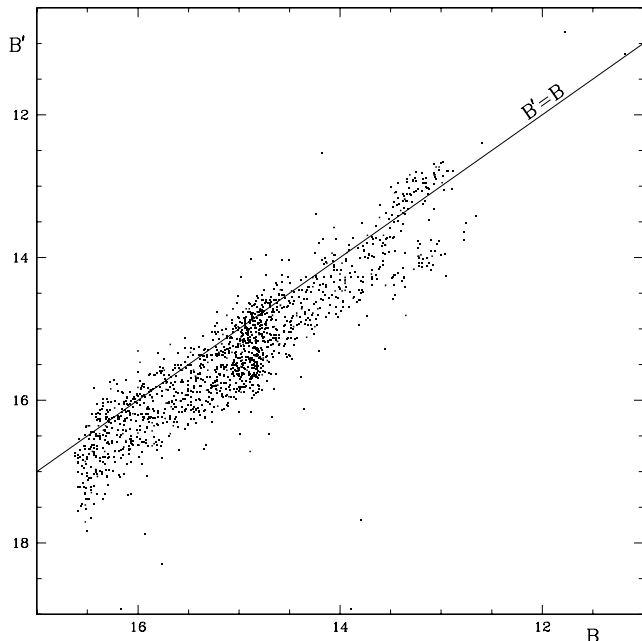


Figure 4. Comparison between the computed magnitude, B' , and the photometric magnitude, B . The absolute calibration of B' is rather arbitrary, but there is a good correlation, with the spread of ~ 1 mag due to variations in the light losses in the fibres as a result of varying observing conditions.

the gravity seems better for the coolest stars, but this may be misleading as some stars might have $\log(g) < 0$ but we did not compute models for such low gravities. The significantly increased spread in $\log(g)$ values in the RR Lyrae box ($0.3 \leq B - V \leq 0.6$) is probably due to radial pulsation (see Section 5.5). The metallicity is determined with an accuracy of ~ 0.2 to 0.4 dex; our choice of steps in metallicity of 0.25 dex is therefore adequate.

The quality of the spectra depends on the amount of light that enters the fibre, which is measured by means of the computed magnitude B' . After normalising to an exposure time of 1000 seconds, it correlates well with the photometric magnitude, B (Fig. 4). The scatter of about a magnitude is largely due to varying observing conditions such as seeing, transparency and airmass, rather than inaccurate centering of the stars. A few stars deviate considerably more from the correlation; some of these are foreground stars, of which the large proper motion difference with respect to the fiducial cluster member stars is responsible for their poor centering and consequent light losses. There is no sign of degradation in the ability to detect signal from the faintest targets.

The computed colour, $B_1 - B_2$ measures the spectral slope, and it is therefore not surprising that it correlates well with the measured temperature (Fig. 5). At $\log(T_{\text{eff}}) > 3.9$ the scatter in the $B_1 - B_2$ colours is somewhat larger than in the $B - V$ colours. On the other hand, the large deviations in the $B - V$ colours seen at $\log(T_{\text{eff}}) \sim 3.8$ are not seen in the $B_1 - B_2$ colours — none of these deviating data are from RR Lyrae stars. The similarity between the two colours suggests that the spectral slope is recorded correctly, and that the sky subtraction in the bluest part of the spectrum is at least roughly correct.

Relationships between colour and temperature have of-

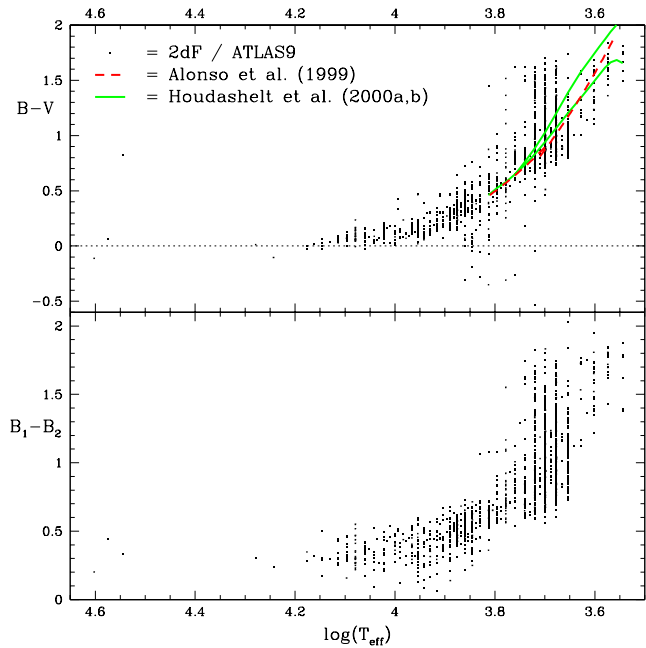


Figure 5. Comparison between the measured temperature, T_{eff} , and the photometric colour, $B - V$ (top panel) and the computed colour, $B_1 - B_2$ (bottom panel). There is a good correlation in both cases; although the scatter in blue $B_1 - B_2$ is larger than in blue $B - V$, the $B_1 - B_2$ does not suffer from the large deviations seen in $B - V$ around $\log(T_{\text{eff}}) \sim 3.8$. In the top panel we also plot empirical relations for red giant stars from Alonso et al. (1999) (dashed) and MARCS-based relations from Houdashelt et al. (2000a,b) for $\log(g) = 0$ (redder curve) and $\log(g) = 1.5$ (bluer curve), all for $[\text{Fe}/\text{H}] = -1$ and reddened by $E(B - V) = 0.11$ mag.

ten been used to derive temperatures for stars from photometry. To compare some of these with our results, we plot in the top panel of Fig. 5 the empirical relation from Alonso et al. (1999) for red giant stars based on the infrared flux method (dashed curve), and the relation from Houdashelt et al. (2000a,b) — which is based on MARCS model atmospheres and empirical calibration — where the redder curve is for $\log(g) = 0$ and the bluer curve is for $\log(g) = 1.5$. We selected the relations for $[\text{Fe}/\text{H}] = -1$, but the differences between the relations covering the metallicity spread in ω Cen are negligible. We applied a reddening of $E(B - V) = 0.11$ mag to these relations as the photometry has not been dereddened. There is good agreement between these relations and our results, in particular for the coolest stars. The redder stars at $\log(T_{\text{eff}}) \sim 3.8$ have lower gravity, which renders both our analysis and the relations derived by Alonso et al. and Houdashelt et al. more uncertain.

The models do not always reproduce all spectral features equally well. Apart from the difficulty with molecular absorption, in particular in the case of M-type and carbon stars, there are a few gravity-sensitive atomic lines which can sometimes be clearly discrepant whilst the remainder of the spectrum is reproduced accurately. Two cases were noted, where the discrepancy is more than a factor two in equivalent width: (i) the Fe I line at 4072 \AA is much weaker than predicted by the model, and (ii) the Ca I line at 4226 \AA and the Fe I lines at 4144 and 4384 \AA are much stronger than predicted by the model. Care should be taken not to mis-

Table 3. Description of the 2dF catalogue of ω Centauri. The column format is given in FORTRAN notation, where the columns are separated by a single space.

| Column(s) | Format | Description |
|-----------|------------|--|
| 1 | I5 | LEID (van Leeuwen et al. 2000) |
| 2-4 | I2 I2 F5.2 | Right Ascension (J2000) ($^{\text{h}} \text{ m } \text{ s}$) |
| 5-7 | I3 I2 F4.1 | Declination (J2000) ($^{\circ} \text{ ' } \text{ ''}$) |
| 8 | F9.5 | Galactic longitude ($^{\circ}$) |
| 9 | F8.5 | Galactic latitude ($^{\circ}$) |
| 10 | F6.3 | B (mag) |
| 11 | F6.3 | $B-V$ (mag) |
| 12 | F6.3 | B' (mag) |
| 13 | F6.3 | B_1-B_2 (mag) |
| 14 | I4 | v_{LSR} (km s^{-1}) |
| 15 | I5 | T_{eff} (K) |
| 16 | F4.2 | $\log(g)$ ($\log \text{ cm s}^{-2}$) |
| 17 | F5.2 | [Fe/H] |
| 18 | I1 | Flag (see Section 4.1) |
| 19 | I1 | If 1: two spectra were taken |
| 20 | I1 | If 1: variable star of RR Lyrae-type |
| 21 | F6.3 | S3839 |
| 22 | F6.3 | S3933[blue] |
| 23 | F6.3 | S3933[red] |
| 24 | F6.3 | CH4300 |
| 25 | F6.3 | Ba4554 |
| 26 | F6.3 | TiO4620 |
| 27 | F6.3 | TiO4760 |

interpret these as due to abundance anomalies. These lines are nevertheless included in the fitting procedure as in many cases there is no discrepancy and they do not by themselves have the ability to significantly alter the overall solution.

4.3 Description of the electronic database

The data products delivered to the community by our 2dF survey of ω Cen comprise of a catalogue of star identifiers with coordinates and photometry and a number of quantities measured from the spectra and discussed in this paper, and the full set of reduced spectra and model fits. They are made available through Centre Données de Strasbourg (CDS), and their format and content are hereby described in brief.

The catalogue has 27 columns (Table 3), and contains 1519 entries. The first column lists the star’s Leiden Identification number (LEID) as used in van Leeuwen et al. (2000) and throughout this paper. Right Ascension and Declination are given in the J2000 system in hours, minutes, seconds and degrees, minutes, seconds notation. The Galactic coordinates are computed from these in the subsequent two columns, and are given in degrees. The optical photometry is taken from van Leeuwen et al. (2000) for B and $B-V$, and computed from the spectrum for B' and B_1-B_2 (see Section 4.1). The radial velocity as measured from the spectrum is corrected for the movement of the observatory with respect to the Sun and for the Sun’s movement with respect to the Local Standard of Rest (LSR). The effective temperature, gravity and metallicity ([Fe/H] by proxy) are measured from the spectrum by fitting ATLAS9 models (see Section 4.1). A flag indicates if a second iteration was performed because possible emission was detected in the hydrogen Balmer series or Ca H+K doublet (see Section 4.1). Another flag is

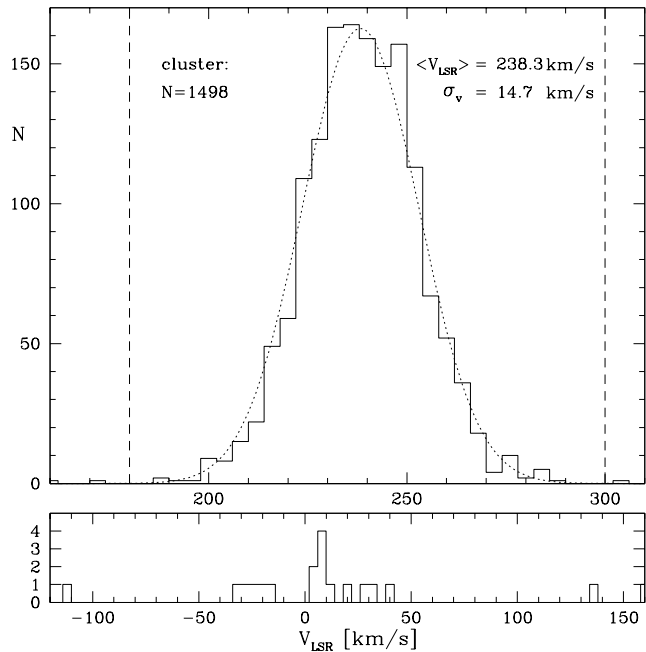


Figure 6. The velocity distribution clearly separates foreground disc stars (bottom panel) from stars in ω Cen (top panel), but this is less obvious for a few stars just outside the bulk of cluster stars as delineated by the vertical dashed lines — these stars might be escaping from the cluster, or they could be cluster binaries or halo stars (see text).

set to 1 if a second spectrum was taken, in which case all measurements are average values. A third flag is set to 1 if the star is a known RR Lyrae-type variable (van Leeuwen et al. 2000). The catalogue further lists the strengths of the CN 3839 Å band, interstellar components in the Ca II H+K lines, CH 4300 Å band, Ba II 4554 Å line, and TiO 4620 and 4760 Å bands (see Sections 5.2, 5.4.2, 5.7.1 and 5.7.3).

Spectra are made available for individual observations, where the file name reflects the star’s LEID number as well as the observation ID from the logbook (Table 1). Each file has four columns and 1024 entries. The first column lists the wavelengths in Å, the second column lists the reduced 2dF spectrum counts, the third column lists the normalised 2dF spectrum, and the fourth column lists the best fitting ATLAS9/SYNTH spectrum (see Section 4.1).

5 RESULTS

5.1 Cluster membership and internal kinematics

The large systemic radial velocity of ω Cen compared to the foreground Galactic disc facilitates the separation of field stars from cluster members (Fig. 6). The radial velocities of the cluster members display a gaussian distribution with a velocity dispersion of $\sigma_v = 14.7 \text{ km s}^{-1}$. Correction for the velocity error of $\sigma_v = 8 \text{ km s}^{-1}$ (Section 4.2) yields a true internal velocity dispersion of $\sigma_v = 12.3 \text{ km s}^{-1}$, slightly smaller than the $\sigma_v = 13.2 \text{ km s}^{-1}$ determined by Pancino et al. (2007) from spectra of a tenfold higher resolving power. The systemic velocity $\langle v_{\text{LSR}} \rangle = 238.3 \text{ km s}^{-1}$ deviates by $+8 \text{ km s}^{-1}$ from the literature value (Meylan et al. 1995), which we attribute to inaccurate absolute calibration of the 2dF

wavelengths. Nonetheless, within our set of measurements we define the realm of cluster members as $180 < v_{\text{LSR}} < 300 \text{ km s}^{-1}$. The field stars are mostly found in the $-30 < v_{\text{LSR}} < 40 \text{ km s}^{-1}$ region, but there are exceptions which may belong to the halo, and it is possible that some field stars have radial velocities within the range of ω Cen.

Of the fifteen targets with $< 90\%$ proper motion membership probability, five are confirmed to be field stars on the basis of their radial velocities. These are: the RR Lyrae variable #27076 ($v_{\text{LSR}} = 160 \text{ km s}^{-1}$), the $P = 1.17 \text{ d}$ eclipsing binary #37328, the late-M type star #44420, the short-period variable star #60026 ($P = 1.5 \text{ hr}$), and #78032. The other ten are radial velocity members, and include the bright stars #16018 and #32029.

The internal kinematics of the cluster show rotation within $r < 0.3^\circ$ at an amplitude of $v_{\text{rot}} \sim 4 \text{ km s}^{-1}$, with the axis of rotation roughly aligned with the Galactic minor axis (Fig. 7b). This is somewhat smaller than found previously by Meylan & Mayor (1986), $v_{\text{rot}} = 8 \text{ km s}^{-1}$, or Reijns et al. (2006), $v_{\text{rot}} = 6 \text{ km s}^{-1}$ (see also van de Ven et al. 2006), and in part due to the angular resolution of 0.1° employed in constructing the maps. The velocity dispersion shows no evidence of spatial variations in excess of 2 km s^{-1} out to $r \sim 0.5^\circ$ (Fig. 7c), but this is due to the limited accuracy of the velocity measurements as well as the $\sim 0.1^\circ$ angular resolution in the core. Hence we are unable to detect the radial gradients in velocity dispersion reported in the literature (Meylan & Mayor 1986; Norris et al. 1997; Reijns et al. 2006).

5.2 Interstellar absorption by ionised gas

In hot stars, with $T_{\text{eff}} \geq 8000 \text{ K}$, the photospheric Ca II H+K lines at 3968 and 3933 \AA are sufficiently weak for the ISM components to be reliably measured (Fig. 8). The ISM component in the K line can be discerned in metal-poor stars as cool as $T_{\text{eff}} \sim 6000 \text{ K}$, but it is difficult to obtain accurate measurements. The same is true for the H line even in hot stars because there it blends with the very strong H ϵ line. Of the classified spectra, 263 are of 231 unique hot stars. Their average not only shows both ISM components very clearly, but each seems to be split in a strong blue-shifted component and a weaker red-shifted component (Fig. 8). The former is entirely consistent with the expected foreground ionised gas in the Galactic disc, but the presence of gas moving at a speed of $\gtrsim 100 \text{ km s}^{-1}$ towards the cluster is unexpected.

We measured the strength of the blue- and red-shifted Ca II K ISM components from the average flux levels, $F_{\lambda_1-\lambda_2}$ (between wavelengths λ_1 and λ_2 in \AA), in the normalised spectrum after subtracting the best model fit, in the following way:

$$S3933[\text{blue}] = F_{3921-3932} - \frac{F_{3916-3921} + F_{3932-3934}}{2}, \quad (5)$$

and

$$S3933[\text{red}] = F_{3934-3939} - \frac{F_{3932-3934} + F_{3939-3950}}{2}. \quad (6)$$

Their variations across the sky are different (Fig. 9), with the blue-shifted component displaying a weak gradient across the face of the cluster, whilst the red-shifted component is clearly concentrated near the cluster centre. This confirms that the blue-shifted component is due to absorption

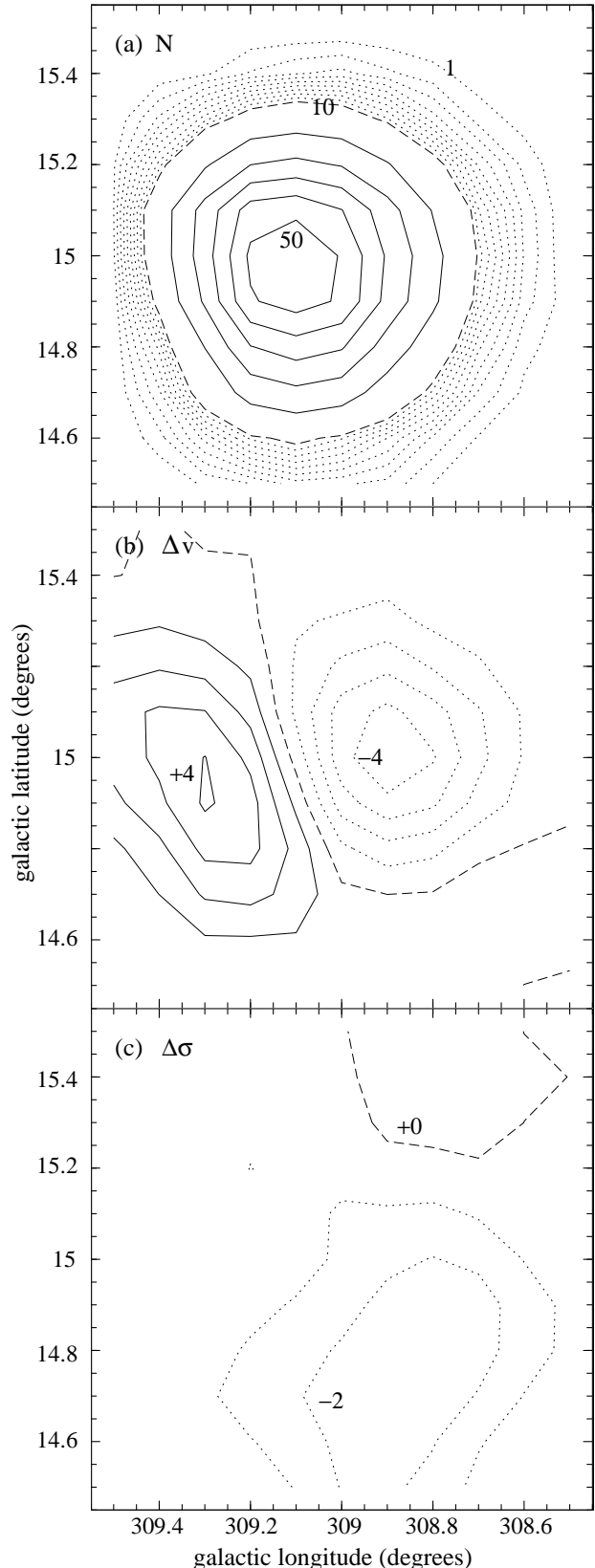


Figure 7. Sky distributions of of: (a) the number of cluster members for which 2dF spectra are analysed, (b) the velocity with respect to the mean velocity of $\langle v_{\text{LSR}} \rangle = 238.3 \text{ km s}^{-1}$, and (c) the velocity dispersion with respect to the mean velocity dispersion of $\sigma_v = 14.7 \text{ km s}^{-1}$. There is evidence for rotation in the inner part, but the cluster periphery appears to be kinematically isothermal.

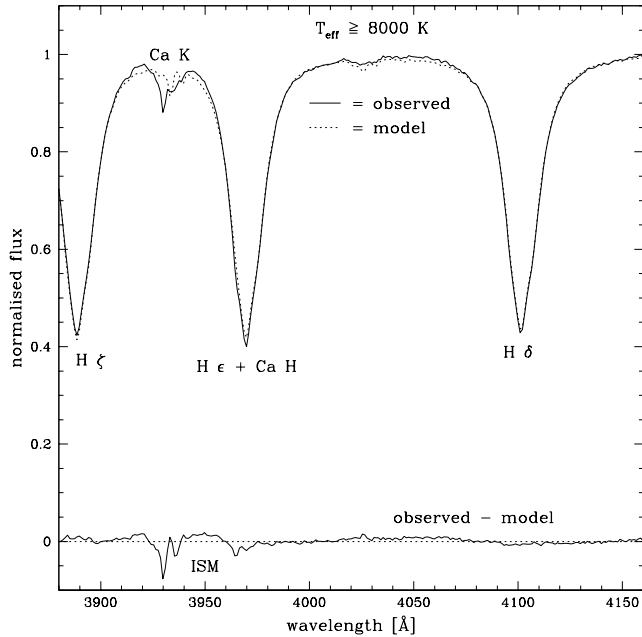


Figure 8. Average of 263 normalised spectra of 231 hot stars, with $T_{\text{eff}} \geq 8000$ K. The average best model (dotted line) fits the Balmer lines perfectly, clearly revealing the interstellar (ISM) component in the Ca II H and K lines; because the stellar spectra have been Doppler-corrected, the ISM components appear shifted with respect to the rest wavelengths of 3968 and 3933 Å.

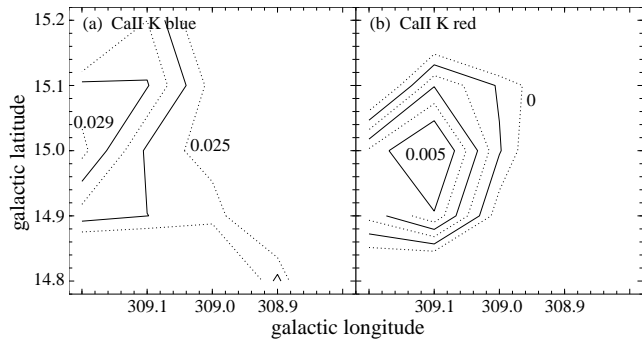


Figure 9. Spatial distribution of ISM absorption in the Ca II K line. The blue-shifted component (a) shows a weak gradient across the face of the cluster, whilst the red-shifted component (b) is concentrated near the cluster centre.

in ionised gas within the Galactic disc, but it hints at the red-shifted component to be associated with gas within the gravitational influence of the cluster.

5.3 Metallicity and the morphology of the Hertzsprung-Russell Diagram

The metallicity distribution of cluster members clearly peaks around $[\text{Fe}/\text{H}] \simeq -1.8$, but the bulk of the stars are spread over a range between $[\text{Fe}/\text{H}] \sim -2.3$ to $[\text{Fe}/\text{H}] \sim -1.3$, with a small distinct peak at $[\text{Fe}/\text{H}] \simeq -0.8$ (Fig. 10). This metal-rich sub-population has spatial and radial velocity distributions which are indistinguishable from those of the bulk of ω Cen members. The uncertainties in the $[\text{Fe}/\text{H}]$ measurements do not allow to identify more sub-populations. The

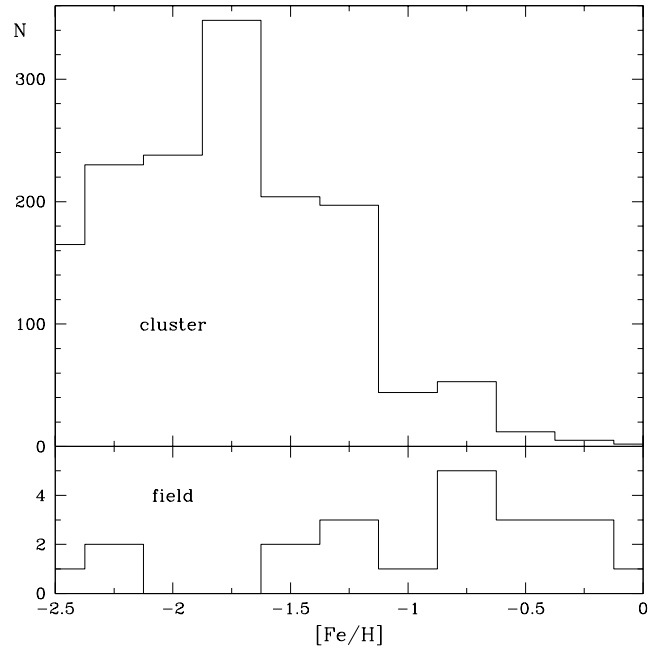


Figure 10. The metallicity distribution of ω Cen (top panel) peaks at $[\text{Fe}/\text{H}] \simeq -1.8$, but the spread is large, $\Delta[\text{Fe}/\text{H}] \sim 1$, and a distinct sub-population around $[\text{Fe}/\text{H}] \simeq -0.8$ is detected. The foreground stars, on the other hand, are mostly found to have $[\text{Fe}/\text{H}] > -1.5$ (bottom panel).

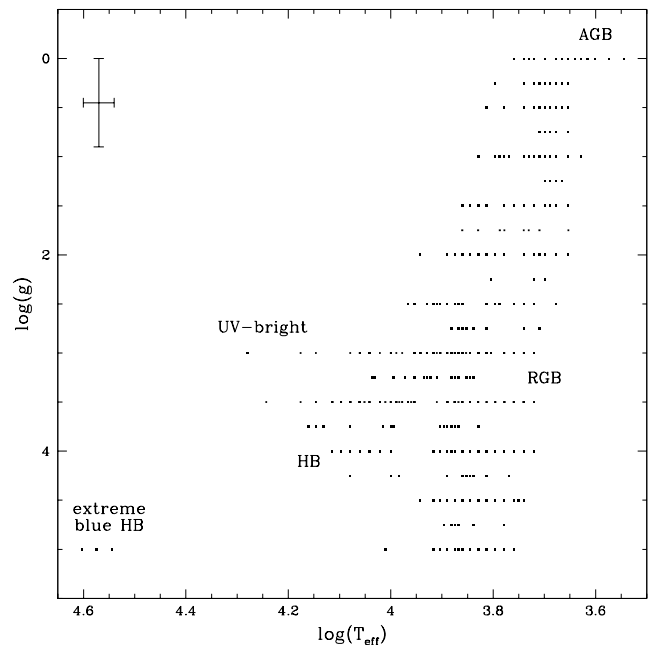


Figure 11. Physical Hertzsprung-Russell Diagram, where gravity (a luminosity indicator) is plotted versus effective temperature. The typical measurement uncertainty is indicated in the top left.

field stars generally have higher metallicities than the cluster members, as expected for the foreground Galactic disc populations, but some metal-poor stars are found in the field and these may belong to the Galactic halo.

The measurement of gravity and temperature enables us to construct a *physical* Hertzsprung-Russell Diagram

(Fig. 11), as opposed to a colour-magnitude diagram. Although the typical measurement error on individual stars is quite substantial (Table 2), the stars nevertheless clearly outline the RGB and HB both in terms of their gravities and temperatures. The gravity is mainly an indicator of stellar radius (and thus luminosity), as the post-main-sequence stars in ω Cen have similar masses: whilst the luminosities span two orders of magnitude, the masses only vary from $\sim 0.8 M_{\odot}$ for RGB stars that have yet to undergo significant mass loss down to $\sim 0.5 M_{\odot}$ for post-AGB and UV-bright stars that will cool to become white dwarfs. As expected, the coolest and largest stars are found near the tips of the RGB and AGB, whilst the extreme blue HB stars are hot and compact.

In order to investigate the dependence of the late stages of stellar evolution on metallicity, the (B, B-V) colour-magnitude diagram is constructed for cluster members in three different metallicity bins: metal-poor, $[\text{Fe}/\text{H}] < -1.9$ (Fig. 12a), intermediate, $-1.9 < [\text{Fe}/\text{H}] < -1.3$ (Fig. 12b), and metal-rich, $[\text{Fe}/\text{H}] > -1.3$ (Fig. 12c). The differences are quite subtle. Individual types of stars are discussed in more detail in subsequent sections.

It seems that the most luminous post-AGB stars are metal-poor, whilst the UV-bright stars are generally more metal-rich (Fig. 12). This may be related to the timescale of evolution of the post-AGB stars, in particular if UV-bright stars are more evolved post-AGB stars. If, on the other hand, UV-bright stars are AGB manqué stars, i.e. stars which evolve from the HB directly towards the white dwarf cooling track bypassing the AGB stage (Greggio & Renzini 1990), then this would imply that the brightest metal-rich stars are on the RGB rather than on the AGB, or in other words the AGB would be dominated by less metal-rich stars.

The clump of stars around $B \sim 14.83$ and $B - V \sim 0.3$ to 0.4 mag (Fig. 12) are mostly RR Lyrae variables; the absence of such clump at $[\text{Fe}/\text{H}] > -1.3$ is commensurate with the notion of RR Lyrae variability being a feature of metal-poor populations. Metal-rich stars do straggle above the HB (around $B \sim 14.6$ mag) more than their metal-poor siblings. Also, the (extreme) blue HB does not seem to be an exclusive feature of the most metal-poor stars, although the poor statistics at $[\text{Fe}/\text{H}] > -1$ hampers deriving a more definitive conclusion.

Theoretical isochrones from Pietrinferni et al. (2004) are plotted in Fig. 12 for $[\text{Fe}/\text{H}] = -1.79$ and -0.97 , respectively. Their standard model without convective overshooting and with solar-scaled abundances is used, for an age of 12 Gyr (cf. Villanova et al. 2007; Stanford et al. 2006a), a distance of 5.2 kpc (cf. Del Principe et al. 2006; van de Ven et al. 2006; Caputo et al. 2002), and reddened by $E(B - V) = 0.11$ mag (Lub 2002). There is rough correspondence between the isochrones and the location of the RGB although the metal-poor model is somewhat too bright. The metal-poor model produces stars near the location of the RR Lyrae instability strip, but the bluer part of the HB is not reproduced. Neither is there evidence in the observed (B, B-V) diagram for the existence of a red clump, predicted for $[\text{Fe}/\text{H}] \gtrsim -1$. This demonstrates the difficulty of theoretical models to reproduce all features seen in globular cluster photometric diagrams.

Surprisingly, the anomalous RGB branch (RGB-a) turns out to be metal-poor, much in contrast with the usual

interpretations of their red optical colours and deep calcium absorption lines. This is investigated in more detail in the next section.

5.4 The first ascent Red Giant Branch (RGB)

Because of the sheer numbers of bright stars, the RGB is a popular place to dissect the stellar populations in globular clusters. The spread in optical colours and magnitudes near the tip of the RGB and the much fainter anomalous branch (RGB-a) are generally considered to be the result of multiple stellar populations, which are expected to show differences in overall metallicity and/or certain elemental abundances.

Some of the fainter stars ($B \sim 16$ mag) have B-V colours in between those of RGB stars ($B - V \gtrsim 0.7$ mag) and those of blue HB stars ($B - V \lesssim 0.2$ mag). We attribute this to photometric errors, as their spectra and temperatures leave no doubt about them being normal RGB stars.

5.4.1 The nature of the anomalous RGB branch

The RGB of metal-rich stars is offset to redder B-V colours by about 0.1 to 0.2 magnitudes (Fig. 12), as expected if their temperatures are slightly reduced because of the enhanced opacity in their mantles and the consequently larger stellar radii. However, the RGB-a does *not* seem to be metal-rich. Selecting the 13 stars with $14.4 < B < 15.1$ and $B - V > 1.3$ mag, these have an average metallicity much in line with the bulk of the ω Cen population: $\langle [\text{Fe}/\text{H}] \rangle_{\text{RGB-a}} = -1.76 \pm 0.43$. However, their temperatures are much lower: $\langle \log(T_{\text{eff}}) \rangle_{\text{RGB-a}} = 3.59 \pm 0.04$ (3867 K). In all but one case, the gravity was determined to be $\log(g) = 0$, which places these stars near the tip of the AGB in the physical HRD (Fig. 11). If they are in fact AGB stars, the ~ 1.6 mag difference in B-band magnitude would naïvely suggest that they lie roughly a factor two further away than ω Cen, placing them in the outskirts of the Galactic bulge. On the other hand, their radial velocities, proper motions and locations on the sky all point at locations within the cluster (van Leeuwen et al. 2000; Pancino et al. 2002). It is much more likely therefore that they do have the bolometric magnitudes of brighter red giants in ω Cen, but that their lower temperatures yield much greater bolometric corrections to their B-band magnitudes. Indeed, RGB-a stars appear much brighter than other cluster stars in the near-infrared than at optical wavelengths (Sollima et al. 2004). Bolometric corrections to optical magnitudes of stars near the tip of the AGB are also relatively large as they have a very low surface gravity (Fig. 5): they are cool and luminous and likely less massive than RGB stars due to mass loss. Therefore, it is possible that some bright AGB stars reach the region of the optical CMD populated by RGB-a stars. We must stress the difficulty of measuring very cool stars ($T < 4000$ K), in particular in distinguishing between a low temperature or a high metallicity.

5.4.2 Nitrogen enrichment

We measured the strength of the strong CN band with a bandhead at 3839 Å, and the strength of the CH band at 4300 Å (the G-band) from the average flux levels, $F_{\lambda_1 - \lambda_2}$

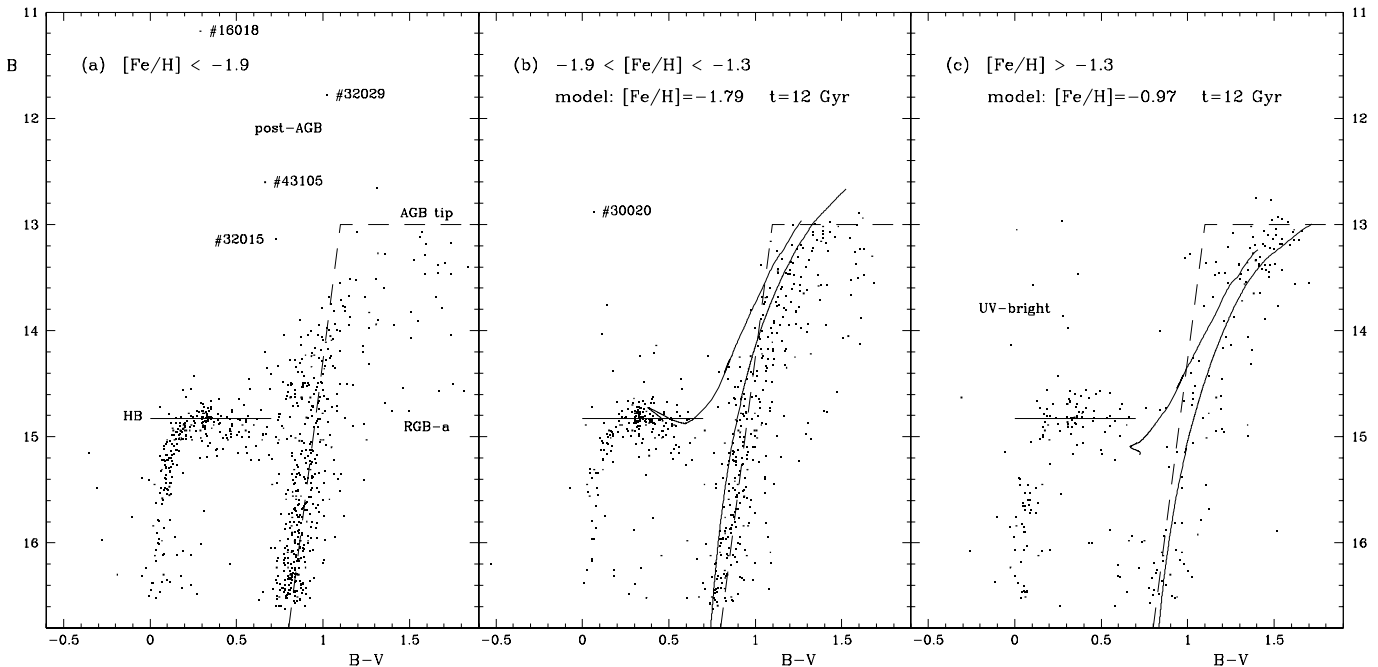


Figure 12. Colour-magnitude diagrams of ω Cen members, for different metallicities. The dashed lines are for reference, delineating the lower RGB and the location of the tip of the AGB; similarly, the solid line indicates the B-magnitude of the RR Lyrae stars (the clump of stars especially clearly visible in the intermediate-metallicity stars in panel b). Theoretical isochrones from Pietrinferni et al. (2004) are plotted for $[\text{Fe}/\text{H}] = -1.79$ and -0.97 , respectively, for an age of 12 Gyr, a distance of 5.2 kpc, and reddened by $E(B - V) = 0.11$ mag (see text for discussion). A few remarkable post-AGB star candidates are labelled.

(between wavelengths λ_1 and λ_2 in \AA), in the normalised spectrum after subtracting the best model fit, following Harbeck et al. (2003):

$$S3839 = -2.5 \log \left(\frac{F_{3861-3884}}{F_{3894-3910}} \right), \quad (7)$$

and

$$CH4300 = -2.5 \log \left(\frac{2F_{4285-4315}}{F_{4240-4280} + F_{4390-4460}} \right). \quad (8)$$

The G-band is visible at higher temperatures than the CN band, which only becomes visible once $CH4300 \gtrsim 0.1$ but this is not guaranteed to be the case until $CH4300 \gtrsim 0.35$ (Fig. 13). There is a clear dichotomy between CN-weak and CN-strong stars, at a given strength of the G-band. This must be due to differences in the nitrogen abundance, as often the temperature, gravity and overall metallicity are the same between stars with and without a strong CN band. However, a weak correlation with overall metallicity is present, with the CN-strong stars being more often metal-rich than the CN-weak stars (Fig. 13). In particular, the strongest CN stars with $S3839 > 0.6$ are almost exclusively metal-rich, with $[\text{Fe}/\text{H}] > -1.3$. This is in agreement with the results from Strömgren photometry by Hilker & Richtler (2000) and the recent work by Kayser et al. (2006) on less evolved stars.

The CN strength shows very little correlation with the position in the colour-magnitude diagram, although it is clear that the nature of RGB-a is *not* related to nitrogen enrichment (Fig. 14). Also, the CN-strong stars seem to avoid the tip of the AGB, which is somewhat surprising given that the tip of the AGB has a relatively larger number of metal-

rich stars (Fig. 13). As for the RGB-a stars, this can be explained if the CN-strong stars are somewhat cooler, yielding greater bolometric corrections to the B-band.

5.4.3 Chromospheric activity

In chromospherically active stars the Ca II H+K lines show line-core inversion due to an emission component (Dupree & Smith 1995). At the moderate resolution of our 2dF spectra, these inversions will not be resolved but instead lead to filling-in of the absorption core. The flag in the catalogue (Table 3, Section 4.1) was used as a criterion to isolate possibly chromospherically active stars (flag=2). Their locations in the colour-magnitude diagram indicate that they are predominantly found amongst red giants (Fig. 15). Indeed, the warmer stars near the bottom of the RGB are expected to have more prominent chromospheres than the AGB stars that rotate slowly or than the HB stars that do not have deep convective mantles. In particular, none of the post-AGB or UV-bright stars are flagged. However, the lower signal at the bottom of the RGB would have led to more spurious flag=2 detections in any case, due to the larger inaccuracies in the absorption line fitting and/or sky background subtraction. In the same way we discard the blue HB stars with flag=2 due to the lower S/N ratio in those faint stars. It is then remarkable that quite many stars near the tip of the RGB and/or AGB are flagged. Their chromospheres may be heated by mechanical energy deposition. Alternatively, it may be too difficult to accurately model the strong Ca II H+K absorption lines in these cool, low-gravity stars.

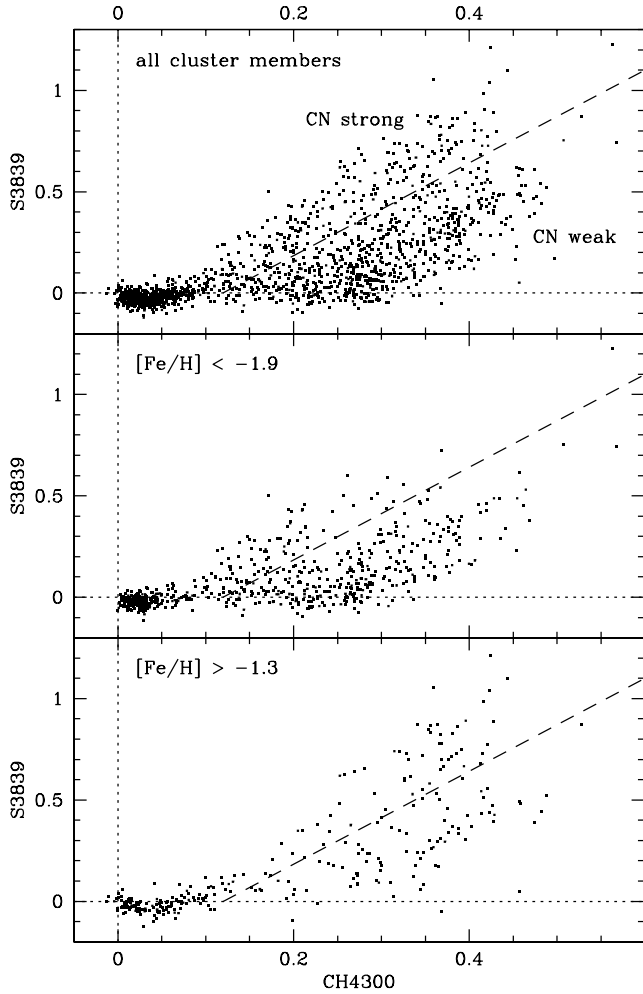


Figure 13. The strength of the 3839 Å band of CN versus that of the 4300 Å (G-)band of CH. For cool stars with a strong G-band, there is a dichotomy in the strength of the CN band.

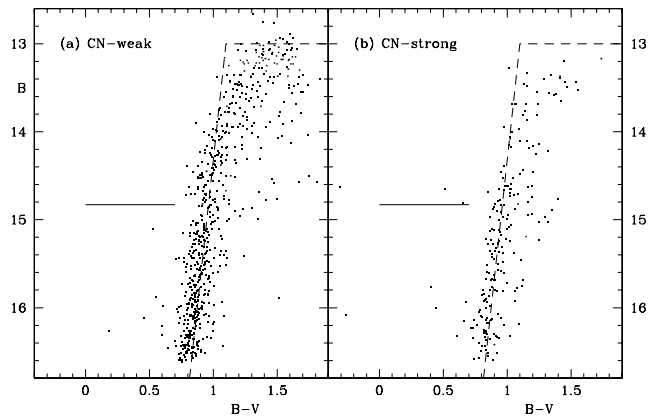


Figure 14. Colour-magnitude diagram of stars with a clear G-band, $CH4300 > 0.15$, split into (a) CN-weak stars and (b) CN-strong stars. These are all red giants, with the odd “blue” star being there due to erroneous photometry.

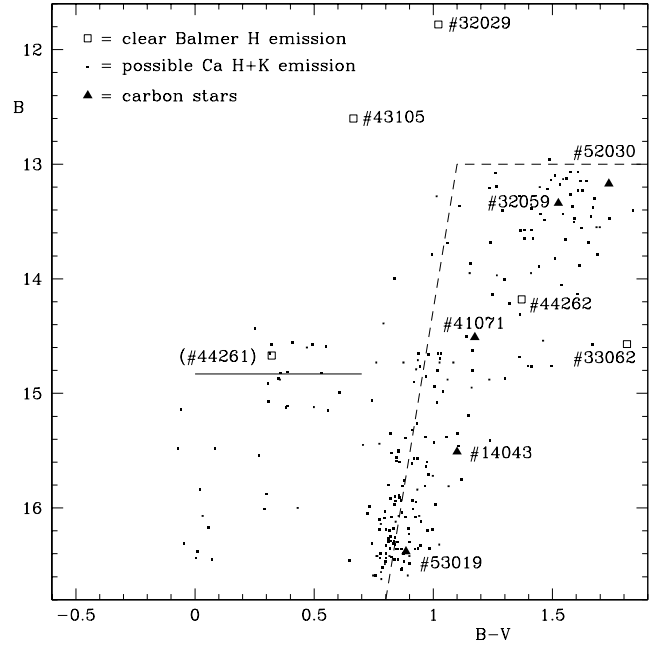


Figure 15. Colour-magnitude diagram of stars with hydrogen line emission (squares), stars with possible Ca H+K emission (dots), and carbon stars (triangles). The H emitters and carbon stars are labelled individually as they are so few — #44261 in fact suffered from contaminating light from the very strong H emitter #44262 (V42) at a distance of 5″.

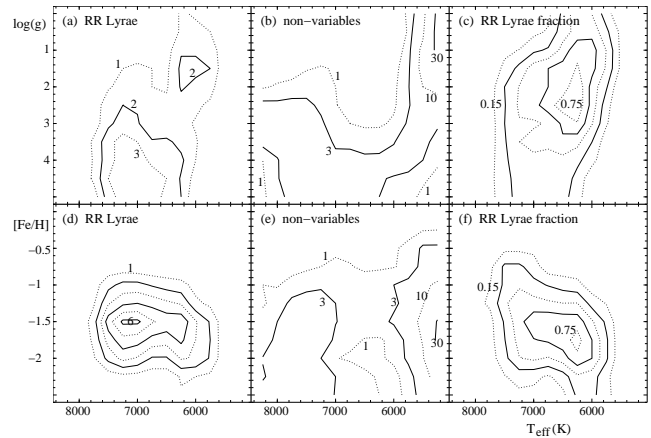


Figure 16. Temperatures, gravities and metallicities of RR Lyrae variables (both in absolute numbers and as a fraction of the total number of stars) and non-variables in ω Centauri.

5.5 The RR Lyrae instability strip

The RR Lyrae variables in ω Cen have a typical temperature of $T_{\text{eff}} = 7000$ K, but a small number of cooler RR Lyrae variables exist with $T_{\text{eff}} = 6000$ K (Fig. 16a). They also differ in gravity, the cooler atmospheres being significantly lighter. They do not, however, differ in metallicity, peaking around the cluster’s bulk metallicity (Fig. 16d). The cooler variables may be on the way up the AGB. There are fewer non-variable stars between 6000 and 7000 K, but there is significant overlap with especially the warm RR Lyrae (Figs. 16b and 16e), whilst a large fraction of the stars around $T_{\text{eff}} = 6000$ K and $\log(g) = 1$ to 2 seem to vary (Fig. 16c).

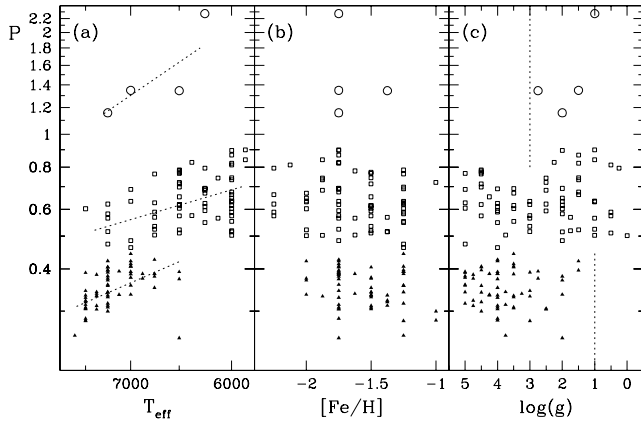


Figure 17. Distributions of RR Lyrae variables in ω Cen over their pulsation periods, as a function of effective temperature, metallicity, and surface gravity. Different symbols are used for stars pulsating in the first overtone ($P < 0.45$ d; filled triangles) or at longer periods ($P > 1$ d; open circles). The dotted lines are meant to guide the eye (see text).

The cooler stars are more likely to vary if they are of low metallicity, whilst the opposite is the case for the warmer variables up to $T_{\text{eff}} \sim 7500$ K (Fig. 16f).

We have spectroscopic variability information for 45 RR Lyrae variables. Although this only comprises one repeat per such star, the time interval is comparable to or larger than their periods and it therefore allows us to make statistical statements about the amplitudes of variability. The differences in stellar parameters deduced from the two epochs are identical to those deduced for other, non-variable stars, except for the variation in gravity which is with $\Delta \log(g) = 1.38$ much larger than that of any other type of star (see Section 4.2). This may be the result of the movement and compression/dilution of the atmosphere in the radial pulsation cycle. Comparison with lightcurves (Weldrake et al. 2007) may reveal phased behaviour of the gravity.

The 49 non-variable stars in the RR Lyrae box (Section 3) for which repeat observations are available still show a relatively large dispersion of $\Delta \log(g) = 1.05$; these stars may be pulsating too, albeit at a lower and hitherto unnoticed level. It is interesting to note that surface-level pulsation modes at milli-mag amplitudes have been predicted to occur in stars at the warm edge of the RR Lyrae/Cepheid instability strip, by Buchler & Kolláth (2001).

The RR Lyrae variables can be divided into RRab-type which pulsate in the fundamental mode at periods between $P \sim 0.45$ and 1 day, overtone RRc-type pulsators with $P < 0.45$ d, and longer-period RR Lyrae variables with periods in excess of a day (Fig. 17). The period increases at lower temperature in all three classes of variables, but at a different rate (dotted lines in Fig. 17a). RRab-types are cooler than RRc-types by ~ 500 K on average. The RRab and RRc-types do not separate in metallicity, although the average metallicity of the RRc-types is slightly higher than that of RRab-types (Fig. 17b). RRab-types and RRc-types span a range in gravities, but the RRab-types reach lower gravities than the RRc-types, and the longer-period RR Lyrae variables also tend to have low gravities (Fig. 17c). This can be understood in terms of the larger radii of longer-period RR Lyrae variables.

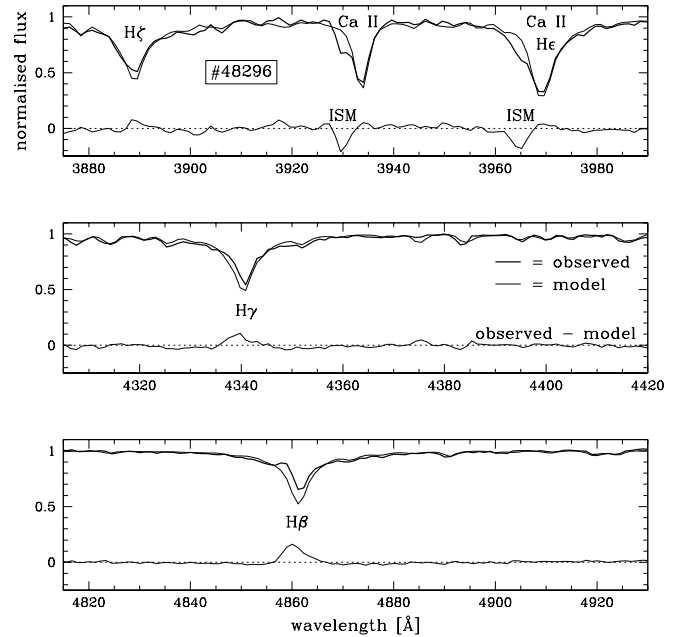


Figure 18. The spectrum of RRa-type variable star #48296. Besides very strong interstellar absorption lines of Ca II it also shows blueshifted Balmer line emission.

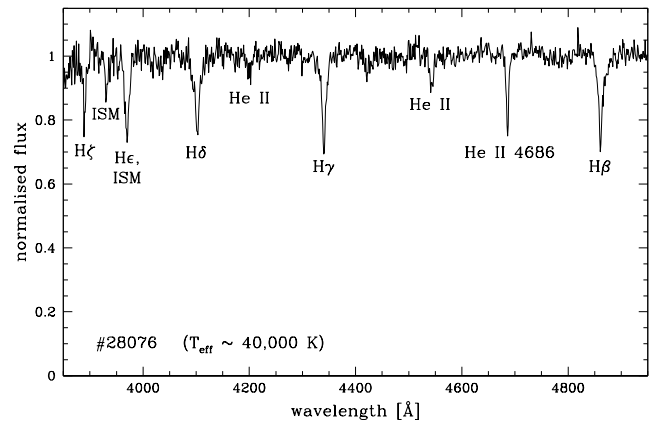


Figure 19. Spectrum of the hottest star detected in our survey, #28076 ($T_{\text{eff}} \sim 40,000$ K). The prominence of the He II 4686 line is clear evidence for its extremely high temperature.

The RRa-type variable star #48296 shows blue-shifted Balmer line emission (Fig. 18). This star belongs to the cool class of RR Lyrae, and has an unremarkable pulsation period of $P = 0.663$ days. Its radial velocity is with $v_{\text{LSR}} = 255$ km s^{-1} fairly high but well within the velocity envelope of the cluster (Fig. 6). It is located at Galactic coordinates $b = 309.1372^\circ$ and $l = 14.9253^\circ$, towards the region of generally high interstellar absorption (Fig. 9). There is a bright 24- μm source at a projected distance of just $10''$ (Boyer et al. 2007). The nature of the Balmer line emission could be due to shocks in the pulsating atmosphere and possibly indicate mass loss.

5.6 Extreme Horizontal Branch stars (EHB)

The HB extends to very high temperatures. Although the bulk of HB stars have $T_{\text{eff}} < 15,000$ K, we detected six stars with $T_{\text{eff}} \geq 15,000$ K, of which two stars have $T_{\text{eff}} > 20,000$ K. All of them appear to have $[\text{Fe}/\text{H}] \geq -1.25$, although there may be systematic uncertainties because the metallicity relies on reproducing the exact shapes of the hydrogen Balmer lines due to the lack of metallic absorption lines at those high temperatures. The metallicity measurements may also be affected by radial gradients within the atmosphere due to radial levitation, diffusive sedimentation, et cetera (Behr et al. 1999). By far the hottest stars are #27010 ($T_{\text{eff}} = 37,500$ K) and #28076 ($T_{\text{eff}} = 40,000$ K). Both stars are assigned the highest value for the gravity, $\log(g) = 5$. They are quite faint as the bolometric corrections to their B-band magnitudes are substantial, and in the case of #27010 this may have led to a slight overestimation of the temperature. The spectrum of #28076 leaves no doubt about its high temperature, displaying strong He II lines (Fig. 19) — these are not included in the models because at such high temperature non-Local Thermodynamic Equilibrium effects become important. It is interesting to note, though, that helium enrichment can explain the high temperatures of EHB stars (Lee et al. 2005).

5.7 The Asymptotic Giant Branch (AGB)

How can we isolate the AGB stars from the much more numerous RGB stars? This is an important question if we are to understand which stars survive the core-helium burning phase and undergo thermal pulses and 3rd dredge-up. To identify and investigate the AGB stars in ω Cen, we look for the coolest stars (Section 5.7.1), long-period variables (Section 5.7.2) and the chemical signatures of dredge-up (Section 5.7.3, where the special case of carbon stars is discussed separately in Section 5.8).

5.7.1 M-type stars

The M type spectral class is defined on the basis of the appearance of TiO bands in the optical spectrum (e.g., Jaschek & Jaschek 1990). The rather abrupt temperature threshold below which TiO forms, the ease with which it forms, the relatively high abundance of oxygen and titanium in most stars (notable exceptions include carbon stars, see Section 5.8), the low excitation of the TiO band transitions and their occurrence throughout the optical spectrum makes M-type stars amongst the easiest to identify. In spite of this, there appear to be only a handful of M-type stars in our sample. The question is whether these are AGB stars, and in what way they are distinct from the other cool giant stars such as the CN-rich stars. With regard to overall metallicity the M-type stars are not particularly metal-rich; only #44262 (V42) may have a somewhat higher metallicity at an estimated $[\text{Fe}/\text{H}] = -1.25$.

To measure the strength of the TiO bands we define two indices, the first of which measures the prominence of the $\lambda 4760$ bandhead:

$$TiO4760 = -2.5 \log \left(\frac{F_{4764-4766}}{F_{4754-4756}} \right), \quad (9)$$

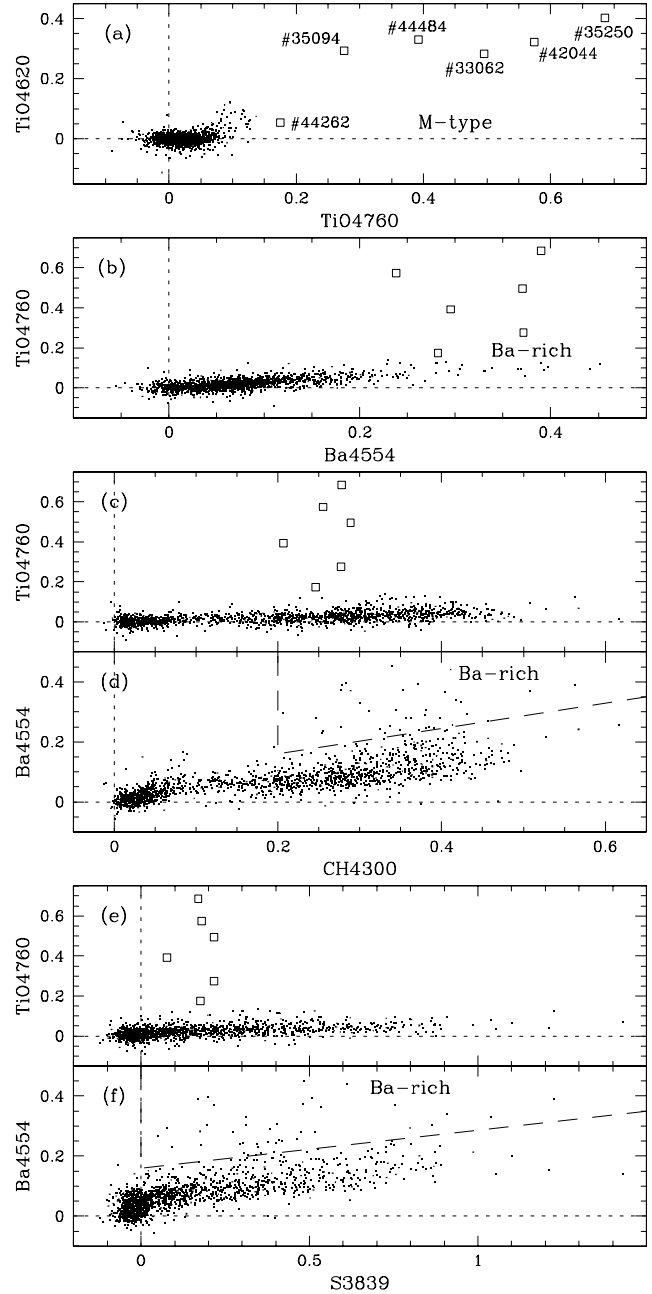


Figure 20. Comparisons between the strength of the TiO and barium absorption, and that of the CH and CN absorption. The M-type stars are indicated with squares and labelled.

and the second of which measures the strength of absorption at either side of the pseudo-continuum around 4620 Å:

$$TiO4620 = -2.5 \log \left(\frac{F_{4590-4592} + F_{4640-4642}}{2F_{4616-4620}} \right), \quad (10)$$

where the average flux levels, $F_{\lambda_1-\lambda_2}$ (between wavelengths λ_1 and λ_2 in Å), are measured in the normalised spectrum. There are a few dozen stars in our sample with detectable TiO absorption, at $TiO4760 > 0.07$ and $TiO4620 > 0.02$ (Fig. 20a). Six stars clearly stand out from the rest, with TiO absorption at a 22 per cent level or more except #44262 (V42) with a TiO 4760 Å bandhead of 8.5 per cent of the

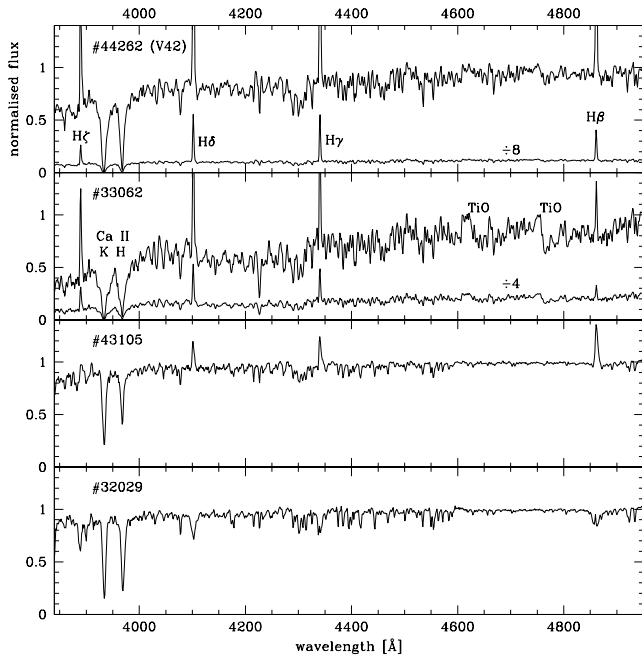


Figure 21. Spectra of the hydrogen Balmer line emission stars detected in our survey. These include the two M-type AGB stars #44262 (V42) and #33062, and the two bright post-AGB stars #43105 and #32029.

continuum; these are identified with different symbols and labelled. While the 4620 Å feature seems to saturate around 30 per cent ($TiO_{4620} \sim 0.3$ to 0.4), the TiO 4760 Å band can reach a depth of more than half the continuum — the most extreme example in our sample is #44420 with indices $TiO_{4760} = 0.92$ and $TiO_{4620} = 0.40$ (not included in Fig. 20 as it is a foreground star).

5.7.2 Pulsation

The coolest and most luminous AGB stars are the most likely stars to undergo strong radial pulsations on timescales of months to years, resulting in large variations in brightness. Indeed, with a period of $P = 149$ days (Sawyer Hogg 1973; Clement 1997; van Leeuwen et al. 2000) the longest-period variable star in ω Cen, V42 (#44262) is one of the few M-type stars in our sample (albeit not the coolest). It also exhibits extremely strong Balmer line emission indicative of the strong shocks that develop in the radially pulsating atmosphere (Fig. 21), shown in detail in a high-resolution spectrum by McDonald & van Loon (2007). The coolest M-type star in our sample, #35250 is also a known long-period variable ($P = 51$ days), but none of the other M-type stars are. Nonetheless, the cool M-type star #33062 is likely to pulsate as it is the only star in our sample besides V42 with strong Balmer line emission (Fig. 21).

The second-longest-period variable with $P = 114$ days, #44277 is cool but not sufficient to show TiO bands strong enough to be classified as an M-type star. The ATLAS9 model fit is quite good and indicates a low temperature, $T_{\text{eff}} = 3750$ K as well as a low metallicity, possibly $[Fe/H] < -2$. It is with $B - V = 1.84$ mag one of the very reddest stars in ω Cen. This star as well as #44262, #33062 and #35250 have recently been found in *Spitzer Space Telescope* images

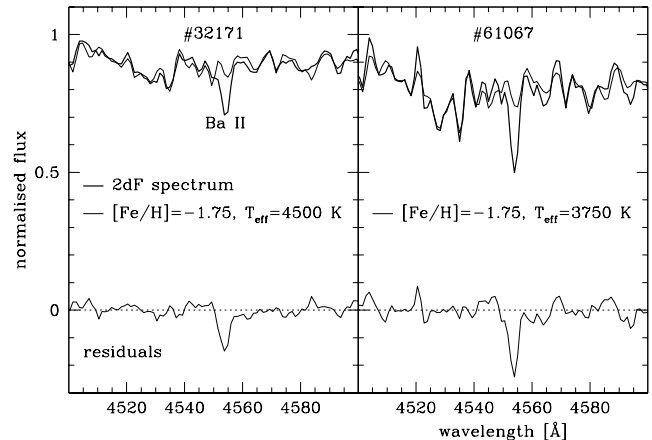


Figure 22. Two examples of barium enrichment.

to have substantial amounts of circumstellar dust (Boyer et al. 2007; McDonald et al., in preparation).

5.7.3 Dredge-up

An s-process element, barium has a strong line at 4554 Å (Ba II). We define the following index:

$$Ba_{4554} = -2.5 \log \left(\frac{2F_{4553-4555}}{F_{4542-4544} + F_{4560-4562}} \right), \quad (11)$$

where the average flux levels, $F_{\lambda_1-\lambda_2}$ (between wavelengths λ_1 and λ_2 in Å), are measured in the normalised spectrum. Many red giant stars show this line, and it becomes stronger in cooler stars. A relatively small number of stars have much stronger barium lines than expected from model atmospheres that do reproduce much of the remainder of the spectrum (two examples are given in Fig. 22). These stars may thus be enriched in s-process elements, possibly as a result of 3rd dredge-up on the AGB. All M-type stars have exceptionally strong barium lines (Fig. 20b).

The strength of the CH absorption extends significantly beyond the narrow range in values of the cool M-type stars (Fig. 20c). Some of these are also enriched in barium (Fig. 20d); none of the stars with CH weaker than that found in M-type stars show any indication of barium enrichment. This clearly suggests that the CH-strongest stars are not simply very cool, but must be enriched in carbon. Alternatively, the M-type stars might be enriched in oxygen, locking away more carbon atoms inside the CO molecule.

The CN bands in M-type stars are even weaker than the CH bands, compared to other cool giants (Fig. 20e). The CN-strong stars may be enriched in nitrogen, as well as carbon. There is no correlation whatever between barium enrichment and strong CN bands (Fig. 21f), suggesting that the nitrogen enrichment is not due to 3rd dredge-up.

Stronger barium lines are found at higher metallicity (Fig. 23, top panels); a distinctive peak in barium strength can be seen to progress from $Ba_{4554} \sim 0.07$ in stars with $[Fe/H] < -1.9$, through $Ba_{4554} \sim 0.09$ in stars with $-1.9 < [Fe/H] < -1.3$, to $Ba_{4554} \sim 0.15$ in stars with $[Fe/H] > -1.3$ (in stars with $Ba_{4554} \lesssim 0.05$ the measurement may be affected by blending lines of other elements). An increased barium abundance amongst the metal-rich sub-

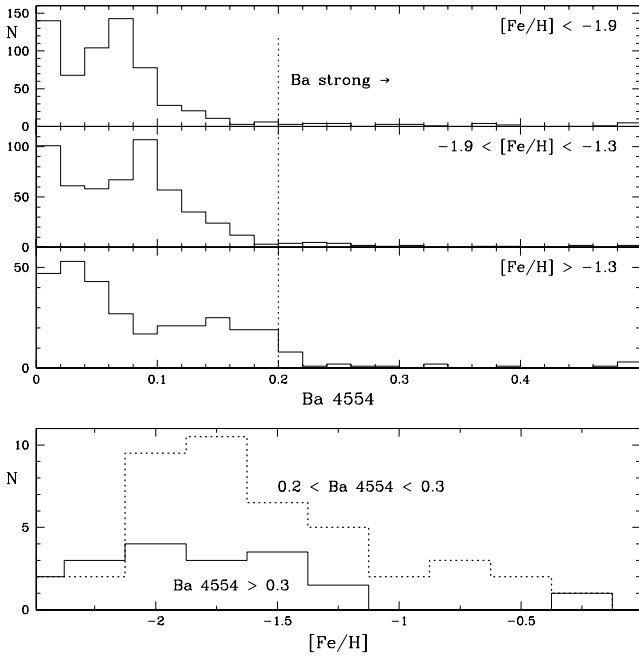


Figure 23. Barium line strength distributions for the metallicity intervals $[\text{Fe}/\text{H}] < -1.9$, $-1.9 < [\text{Fe}/\text{H}] < -1.3$ and $[\text{Fe}/\text{H}] > -1.3$ (top panels), and metallicity distributions of the Ba-strong stars with $0.2 < \text{Ba}4554 < 0.3$ (dotted) and $\text{Ba}4554 > 0.3$ (solid) in the bottom panel. Although metal-rich stars have stronger barium lines, there is little evidence for a metallicity bias of the Ba super-enhancement.

populations in ω Cen is well documented, and likely due to enrichment by the ejecta from AGB stars over a period of star formation lasting more than a Gyr (Smith et al. 2000). However, the Ba-strong stars with $\text{Ba}4554 > 0.2$ show a very different picture (Fig. 23, bottom panel). The metallicity distributions of these Ba-strong stars do not differ very much from the overall cluster metallicity distribution (Fig. 10). We will refer to this phenomenon as barium “super-enhancement”, to distinguish it from the metallicity-correlated chemical pre-enrichment seen at $\text{Ba}4554 < 0.2$. Barium super-enhancement seems to be common amongst stars belonging to the bulk of ω Cen’s population with $[\text{Fe}/\text{H}] \sim -1.8$, and *not* a feature specific to a metal-rich sub-population. A plausible explanation would therefore be that barium super-enhancement is due to dredge-up of s-process elements in the stars themselves.

The Ba-strong stars as defined in Fig. 20f are cool and luminous (Fig. 24); if the barium is enriched due to 3rd dredge-up, then these stars delineate the thermal-pulsing AGB. The reason why the Ba-strong sequence is a little redder and fainter in the B-band than other, Ba-weak stars may be a result of larger bolometric corrections to the optical photometry. The M-type stars are also relatively faint in the B-band, probably for the same reason. In fact, four of the six M-type stars are on the RGB-a sequence (Fig. 24).

5.8 Carbon stars

Apart from many stars which show the 4300 Å CH band and the 3839 Å CN band, a few stars also show absorption by C_2 molecules around 4700 Å (which form part of the Swan

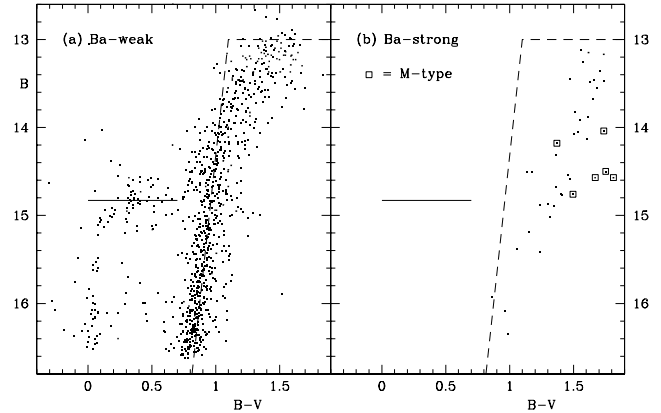


Figure 24. Colour-magnitude diagram of (a) Ba-weak stars and (b) Ba-strong stars. The M-type stars are also indicated (squares).

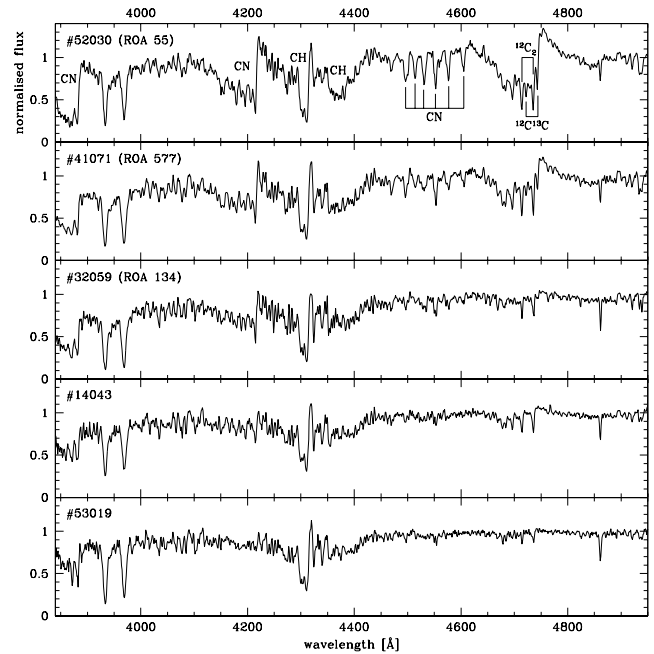


Figure 25. Spectra of the carbon stars detected in our survey. These are defined as stars with absorption by C_2 molecules (most notably around 4700 Å), not just CN and/or CH.

system). Whereas CH and CN are seen in cool, oxygen-rich stars including the Sun, C_2 molecules only form when the carbon-to-oxygen ratio is larger than unity. They have been called “cool CH stars” in the past, but this is a misnomer as many cool CH stars do not show C_2 bands. We prefer to refer to the stars showing C_2 bands as “carbon stars”. Four carbon stars were known in ω Cen: ROA 55 (Harding 1962), ROA 70 (Dickens 1972; Wing & Stock 1973), ROA 279 (Bond 1975), and ROA 577 (Cowley & Crampton 1985). Another carbon star, ROA 153 has the wrong proper motion (Woolley 1966) and radial velocity (Smith & Wing 1973) to be a cluster member.

We obtained spectra of ROA 55 (#52030) and ROA 577 (#41071), and discovered three more carbon stars: #32059 (ROA 134), #14043 and #53019 (Fig. 25). The measured stellar parameters were $T_{\text{eff}} \sim 4500$ K, $\log(g) \sim 1.5$ and $[\text{Fe}/\text{H}] \sim -2.5$ to -2 , respectively, but these are unreliable

because the model does not reproduce the C₂ and strong CN bands. The three new carbon stars would have been inconspicuous on the objective prism plates that were used to survey ω Cen in the past, and they could only be found by a systematic spectroscopic survey. Especially the last two stars only show moderate enhancement of the CN and CH bands. We may thus anticipate that the total number of (weak) carbon stars in ω Cen may lie around ~ 30 .

The carbon stars are found along the entire length of the red giant branch (Fig. 15). At least the fainter carbon stars are therefore more likely to have had their carbon abundances enhanced through the process of mass transfer from a close carbon star companion many Gyr ago. The three brightest carbon stars show also the 4722+4744 Å ¹²C:¹³C heavy-isotope version of the 4714+4735 Å C₂ lines; the ¹²C:¹³C:C₂ strength ratio is very high in the brightest and reddest carbon star #52030 (ROA 55). This suggests a ¹²C:¹³C ratio $\ll 10$, which clearly points at the s-process in an AGB carbon star to have been responsible for the bulk of the carbon found in this star. The Ba II 4554 Å line is strongest in the carbon stars with the strongest C₂ and CN bands, though, suggesting a link between the carbon enrichment and an enhancement of the barium abundance.

5.9 Post-AGB and UV-bright stars

Stars brighter than the HB but not on the upper RGB or AGB are candidate post-AGB stars (Fig. 12). For a handful the evidence for this is quite convincing. Line emission is seen in #43105 (V29) and #32029 (Fig. 21), indicative of circumstellar material reminiscent of a planetary nebula. The line emission in #32029 appears as line core inversions because of the lower contrast against the brighter underlying stellar photospheric emission as compared to #43105. Very faint line emission might be present in the luminous yellow supergiant #16018 as well (Fig. 26), but it is at a level at which the accuracy of the model fit cannot be guaranteed. In #43105 and especially #32029 many absorption lines including the Ba II line at 4555 Å are stronger than in the model, which reproduces the calcium doublet and various other lines rather well (Fig. 26). Indeed, Gonzalez & Wallerstein (1994) found CNO and s-process enhancements in the atmospheres of all these three luminous UV-bright stars, confirming their post-AGB nature.

The fainter UV-bright stars do not show obvious line emission. They are all confirmed proper motion and radial velocity members. Landsman et al. (1992) argue that these stars are less luminous than one would expect post-AGB stars to be, and they may instead have evolved off the early-AGB (before the onset of thermal pulses) or HB before climbing the AGB (AGB Manqué). This is consistent with the findings of Gonzalez & Wallerstein (1994), who did not detect any peculiarities in the chemical abundances of two of these stars, #32015 (ROA 342) and V48. The absence of line emission may then be due to weaker mass loss, or because of longer evolutionary timescales leading to the dispersal of circumstellar material before it is ionised.

6 DISCUSSION

6.1 Late stages of evolution of metal-poor stars

The late stages of stellar evolution determine the fate of a star and its remnant (if any), as well as the return of nuclear processed material into the ISM. Mass loss is a critical factor in this as it truncates stellar evolution. The evolution of stars of nearly solar mass is particularly sensitive to the time-dependence of the mass loss, as the mass loss during the RGB determines how many thermal pulses on the AGB it will undergo — if any (for a comprehensive review of stellar evolution in globular clusters see Renzini & Fusi Pecci 1988).

6.1.1 Horizontal Branch stars and RR Lyrae variables

The core-helium burning phase is a valuable diagnostic intermediate phase in post-main sequence evolution as the star's properties during this phase depend critically on the core mass and mantle mass and composition. The core mass is similar for all stars undergoing the helium flash at the tip of the RGB, whilst the mantle mass depends on the integrated mass loss on the RGB. Stars with thinner mantles become bluer HB stars, but a lower metallicity has a similar effect as it reduces the opacity in the mantle rendering a hotter photosphere. Indeed, ω Cen displays a prominent metal-poor blue HB (Fig. 12a, at $15 < B < 15.6$ mag) where there is a gap for metal-rich stars (Fig. 12c). Metal-rich stars do become blue HB stars though (at $B \gtrsim 15.5$ mag), possibly as a result of accelerated evolution if enhanced in helium (Lee et al. 2005) or as a result of mass loss on the RGB. A smaller, bluer gap is present for metal-poor stars (at $B \sim 15.7$ mag). Differences in atmospheric structure are expected as the ionization balance changes. This can be accompanied by diffusion leading to surface metal enhancement, possibly explaining the relatively high metallicity of the hottest (EHB) stars in our sample, although metal-poor stars appear to populate the blue tail too (at $B \gtrsim 15.8$ mag).

Depending on the mass and mantle structure, some HB stars occupy the RR Lyrae instability strip. The pulsation properties thus contain information related to the RGB mass loss. For instance, Butler et al. (1978) suggest that some metal-rich, later-spectral type RR Lyrae may be $\sim 0.1 M_{\odot}$ less massive, possibly due to heavier mass loss on the RGB. We do not find such cooler metal-rich RR Lyrae, but we do find cool RR Lyrae stars with longer pulsation periods ($P > 1$ d) and lower surface gravities — these may already have evolved off the zero-age HB and be moving up the AGB, and it is possible that mass loss on the HB has further depleted their mantles.

Brighter HB stars could signal helium enrichment (e.g., Sweigart 1997). HB stars about 0.2 mag brighter than the RR Lyrae locus are found amongst relatively metal-rich stars (Fig. 12). On the other hand, Sollima et al. (2006) show that metal-intermediate RR Lyrae stars are fainter, and that they are fully consistent with a normal helium abundance. Indeed, He-rich HB stars are hotter and hence do not occupy the RR Lyrae instability strip (Lee et al. 2005).

There is some variation amongst the warmer RR Lyrae, where the fraction of overtone pulsators increases and where stars are found which have not so far been recognised as RR Lyrae but whose surface gravities vary between repeat

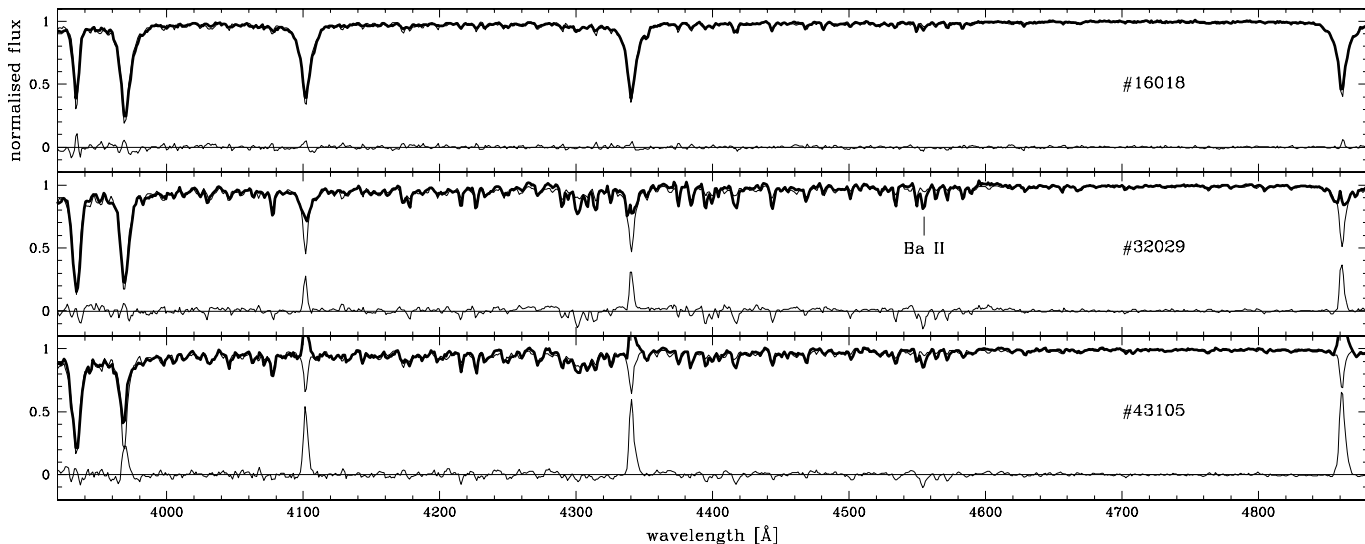


Figure 26. Spectra of post-AGB stars #16018, #32029 and #43105 (bold lines), together with the model fits (thin lines) and residuals.

measurements more than those of stable stars elsewhere in the HRD — these might be the low-amplitude pulsators predicted by Buchler & Kolláth (2001).

6.1.2 Asymptotic Giant Branch stars and dredge-up

HB stars with sufficiently massive mantles will climb the AGB. The AGB blends with the RGB, and in blue-visual colour-magnitude diagrams the tip-AGB stars are no longer the brightest because they will be exceedingly cool and therefore emit an increasing portion of their light at longer wavelengths. The small group of M-type stars in our 2dF sample are redder but fainter than the upper red giant branch, and most fall on the RGB—a anomalous red giant branch. Our *Spitzer Space Telescope* infrared atlas, however, clearly shows that they are the most luminous stars in the cluster (Boyer et al. 2007; McDonald et al., in preparation). We thus identify the M-type stars as tip-AGB stars. They appear to be nitrogen-poor, as the strength of the CN bands is very modest at a given strength of the G-band (CH). The metallicities of these very cool stars are difficult to determine reliably, but they do not appear to be particularly high. The most luminous AGB stars in ω Cen could have their origin in the most primitive sub-population in the cluster. Evidence for dredge-up of the products of nucleosynthesis in thermal pulses would unambiguously confirm the AGB nature.

We have been able to isolate stars that are super-enriched in barium, above the level resulting from pre-enrichment by a previous generation of AGB stars. In the latter, comprising the majority of stars in which barium lines are seen, the 4554 Å barium line simply increases in concert with the CN and CH band strength and with overall metallicity. This is expected as AGB stars with masses $1.5 < M < 3 M_{\odot}$ produce a large amount of Ba and C (Smith et al. 2000; Herwig 2005). The super-Ba-rich stars, though, do not show such correlation (Figs. 20 & 23), suggesting that low-mass, metal-poor stars may be efficient in enriching their photospheres with s-process elements without showing a marked carbon enrichment. The super-Ba-rich are generally the coolest and brightest stars in the cluster,

and include the M-type stars (Fig. 24). We thus conclude that the super-Ba-rich stars in general, and the M-type stars in particular, have undergone at least one thermal pulse, but that this was not generally sufficient to raise the carbon-to-oxygen ratio above unity. Perhaps a process is operating akin to the cool bottom processing occurring in RGB stars, depleting carbon by burning it through the CNO cycle at the bottom of the convective mantle when it dips into the hydrogen-burning shell (Wasserburg, Boothroyd & Sackmann 1995; Boothroyd & Sackmann 1999).

Amongst the many stars with strong CN and CH bands we recover all three known, and discover three new genuine carbon stars on the basis of the presence of C_2 in their atmospheres. They are Ba-rich and ^{13}C -rich, which suggests dredge-up on the AGB. The faintest carbon star is unlikely to be on the AGB though, and the ^{13}C enhancement has also been explained by Origlia et al. (2003) in terms of cool bottom processing and extra mixing on the RGB. Whether or not the carbon stars that we find in ω Cen today are the product of self-enrichment or of mass transfer from an erstwhile more massive carbon star companion, we do find carbon stars near the very tip of the AGB, and it is likely that these will produce dust of a carbonaceous nature, which will enter the ISM.

6.1.3 Mass loss and post-AGB objects

That said, the direct evidence in our medium-resolution spectra for mass loss is meager. Shocks due to strong stellar pulsation are found in two M-type AGB stars in the form of hydrogen line emission, but echelle spectra are needed to detect outflow motion. An important question is whether the well-known paradigm of pulsation-initiated, dust-assisted mass loss necessarily comprises most of the mass shed by metal-poor low-mass stars. Such stars spend most of their time being too warm for pulsations to develop and for an extended molecular atmosphere and circumstellar dust to form. Yet these stars are likely to have a chromosphere, which might provide an alternative means for driving mass loss (Schröder & Cuntz 2005; McDonald & van Loon, in

preparation). Our spectra do show hints of chromospheric emission in the Ca H+K doublet along much of the red giant branch, but this diagnostic is too sensitive to other effects to be reliably applied to our medium-resolution spectra.

We identified post-AGB stars in ω Cen on the basis of their blue colours, high luminosities and in a few cases hydrogen line emission (besides proper motion and radial velocity membership). Like the M-type AGB stars they appear to be metal-poor (Fig. 12). We speculate that metal-poor stars might suffer less mass loss on the RGB and hence climb higher on the AGB, ultimately becoming post-AGB stars. This is consistent with the copious dust production and presence of a carbon-rich planetary nebula in the extremely metal-poor globular cluster M15 (Boyer et al. 2006). Metal-rich clusters would be predicted to host more post-early-AGB and post-HB stars, as stronger mass loss on the RGB would have reduced their mantles enough to prevent them from reaching the thermal-pulsing part of the AGB. This is corroborated by our data, which suggest that the less luminous UV-bright stars are relatively metal-rich. On the other hand, however, metal-rich clusters, with $[\text{Fe}/\text{H}] \simeq -0.7$, are known to host more luminous AGB stars undergoing long-period variability which suggests that they have larger core masses (Frogel & Elias 1988). Either these clusters are younger by several Gyr, or mass loss on the RGB was not stronger than for clusters with $[\text{Fe}/\text{H}] \sim -2$ to -1.5 (cf. Renzini & Fusi Pecci 1988).

6.2 Cluster formation and evolution

The details of the formation and evolution of ω Cen are imprinted in the chemical and dynamical properties of its multiple populations. We briefly discuss the results from our analysis in this context.

6.2.1 The nature of the multiple stellar populations

The isolation and characterization of stellar populations of different age and composition is hampered by the high level of degeneracy between metallicity and temperature in photometry and low to medium-resolution spectroscopy. Below ~ 4000 K much of the atomic and molecular opacity increases both with higher abundance and lower temperature. This could explain why our spectroscopic analysis indicates that the cool RGB-a stars may have “normal” abundances, $[\text{Fe}/\text{H}] \sim -1.7$, where other published work indicates that the RGB-a is considerably more metal-rich. Such discrepancies may also arise from spectroscopic missions such as *GAIA*, so it is important to be aware of the ways in which a different methodology could yield different answers.

Metal-rich stars tend to be identified through calcium/colour methods not by means of a full spectral synthesis. We do not constrain the solutions by using priors, but obtain the best fit to the observed spectrum by varying T_{eff} , $\log(g)$ and $[\text{Fe}/\text{H}]$. Neither Origlia et al. (2003), Sollima et al. (2005), Stanford et al. (2006a) or Villanova et al. (2007) fit T_{eff} to the spectra but instead use photometry to constrain it (Villanova et al. also constrain $\log(g)$ in this way). Their results are not always consistent, for instance Villanova et al. (2007) find $[\text{Fe}/\text{H}] = -1.1$ for the subgiants that evolve into the RGB-a, which is 0.5 dex lower than Pancino et al. (2002) find. The latter authors do estimate T_{eff}

Table 4. Comparison between the solutions for T_{eff} and $[\text{Fe}/\text{H}]$ with the original procedure (subscripts “0”) and when fixing the value for T_{eff} to that closest to the value derived from the Alonso et al. (1999) colour- T_{eff} relation (subscripts “a”), for a selection of stars with colours like RGB-a stars: $14.4 < B < 15.1$ and $B - V > 1.3$.

| LEID | $B - V$ | $T_{\text{eff,a}}$ (K) | $[\text{Fe}/\text{H}]_a$ | $T_{\text{eff,0}}$ (K) | $[\text{Fe}/\text{H}]_0$ |
|-------|---------|------------------------|--------------------------|------------------------|--------------------------|
| 32149 | 1.302 | 4169 | -1.50 | 4000 | -1.75 |
| 18046 | 1.319 | 4147 | -1.25 | 4000 | -1.50 |
| 69027 | 1.399 | 4048 | -1.50 | 4000 | -1.375 |
| 23031 | 1.347 | 4112 | -1.25 | 4000 | -1.25 |
| 77010 | 1.351 | 4107 | -2.00 | 5000 | -1.00 |
| 48321 | 1.360 | 4096 | -2.00 | 3750 | -2.25 |
| 54022 | 1.412 | 4033 | -1.50 | 4000 | -1.50 |
| 48323 | 1.461 | 3975 | -1.75 | 3750 | -2.00 |
| 60058 | 1.475 | 3958 | -1.50 | 4000 | -1.50 |
| 44484 | 1.497 | 3933 | -2.25 | 3500 | -2.50 |
| 35094 | 1.670 | 3746 | -1.75 | 3500 | -2.00 |
| 35250 | 1.752 | 3663 | -1.75 | 3500 | -2.25 |
| 33062 | 1.813 | 3604 | -2.25 | 3500 | -2.00 |

directly from their spectra by imposing excitation equilibrium on a set of iron lines. They analysed three metal-rich and three intermediate-metallicity stars, and find temperatures around 4000 K, i.e. not extremely cool. Our own analysis suggests that what look like RGB-a stars may in fact be cool but metal-poor. As our data do detect a metal-rich sub-population across the upper HRD, we tentatively conclude that our low $[\text{Fe}/\text{H}]$ values for the RGB-a stars may point at a problem inherent to the spectroscopic technique (or sample selection).

To investigate the extent to which the freedom in our method may produce less realistic solutions than methods in which some of the parameters are set *a priori*, we have run our model fitting procedure on the 13 RGB-a candidate stars with $14.4 < B < 15.1$ and $B - V > 1.3$ but constraining the solution for T_{eff} to that closest to the value predicted by the Alonso et al. (1999) colour- T_{eff} relation. The results are listed in Table 4 (with subscripts “a”) and compared to the solutions obtained with the unrestrained procedure (with subscripts “0”). The differences are generally small, only one step in temperature and/or metallicity. This is because the original procedure yields temperatures that are already in fair agreement with the colour- T_{eff} relations. Although in six cases the value for $[\text{Fe}/\text{H}]$ has increased by constraining the value for T_{eff} , in three cases it has actually decreased. The formerly most metal-rich star in this selection, #77010 has become one of the most metal-poor stars. This is the only star for which the value for the gravity changed: from $\log(g) = 2$ to become 0. We conclude that setting constraints on the available parameterspace informed by photometry has a systematic but not very dramatic effect on the metallicity determinations, and does not necessarily result in higher metallicities for stars in the RGB-a portion of the (B, B-V) colour-magnitude diagram.

Irrespectively, our selection of RGB-a stars is not uniformly strong in CN. In fact, some M-type stars are found on the RGB-a. These are cool, which would have made CN bands strong, but clearly oxygen-rich, which agrees with the observed weak CN bands. Pancino et al. (2002) and Origlia et al. (2003) indeed find that RGB-a stars have so-

lar $[\alpha/\text{Fe}]$, and suggest the delayed enrichment with iron by supernovae of Type Ia. These stars must then also be pre-enriched in s-process elements by a previous generation of AGB stars. This scenario is confirmed by the increasing strength of the barium line with increasing metallicity (Fig. 23), which would be more consistent if the RGB-a stars were metal-rich. The CN-rich stars are generally metal-rich as well as nitrogen-enriched — compared to M-type stars and CN-weak stars in general. The elevated levels of nitrogen must be due to pre-enrichment in these stars. The helium-rich stars are probably related to this episode of formation from gas enriched by massive stars. Different evidences suggesting a large helium enhancement of RGB-a stars have been put forward (Norris et al. 1996; Sollima et al. 2005; Lee et al. 2005; Villanova et al. 2007).

We conclude that care has to be exercised in studying the RGB-a, as extreme AGB stars may mimic RGB-a optical colours and magnitudes. In combination with the difficulty in modelling accurately the stellar atmospheres and spectra of cool stars and measuring the stellar properties from low-resolution spectra, this explains our general finding that RGB-a stars may be metal-poor whilst all other evidence suggests that (true) RGB-a stars are metal-rich.

6.2.2 Gas retention and accretion

Our data independently confirm some of the internal kinematic properties of ω Cen as reported in the literature, in particular the rotation of its core (Merritt et al. 1997; van Leeuwen & Le Poole 2002; Reijns et al. 2006). We do not find evidence for different kinematics of the various sub-populations, nor for a different spatial distribution. Sollima et al. (2007) find that the blue (intermediate metal-rich) main sequence stars are more concentrated towards the cluster centre, confirming an earlier result obtained by Norris et al. (1997) and for the metal-rich stars by Pancino et al. (2003). Norris et al. (1997) and Ferraro et al. (2002) also suggested a difference in kinematics between the metal-poor and metal-rich populations, but van de Ven et al. (2006) and Pancino et al. (2007), as well as our own data, show that there is no evidence for such difference thus removing the strongest evidence for a merger scenario to explain the multiple populations in ω Cen. The more likely scenario for producing the multiple populations in ω Cen thus remains the prolonged or episodic star formation as a result of gas retention or accretion in the immediate proto-cluster environment, possibly as part of a once larger system (cf. Bekki 2006).

We obtained a crude map of the diffuse ionized medium in the foreground of ω Cen, demonstrating the potential of using the many blue HB stars in metal-poor globular clusters for probing the ISM. We also tentatively detect, in both the H and K components of the Ca II doublet, what appears to be a high-velocity cloud moving towards ω Cen at a (projected) velocity close to 200 km s^{-1} with respect to the systemic motion of the cluster. This is faster than the expected free-fall velocity, which would be $\sim 42 \text{ km s}^{-1}$ to reach the inner half-mass radius of $\sim 6 \text{ pc}$ if the total mass is $\sim 2.5 \times 10^6 M_{\odot}$ (van de Ven et al. 2006). The cluster is therefore likely to pass through it and leave it behind. Slower encounters could lead to capture of interstellar clouds, and we speculate that accretion events could in the distant past

have led to the formation of the chemically distinct sub-populations that we see today.

7 SUMMARY OF CONCLUSIONS

We obtained medium-resolution optical spectra for > 1500 proper motion members of the Galactic globular cluster ω Centauri, making a particular effort to sample the entire upper part of the optical colour-magnitude diagram (not just where most stars are). We measured the radial velocity, effective temperature, metallicity and gravity in an automated fashion by fitting synthetic spectra based on model atmospheres. We present a catalogue which contains these data as well as the measured line strengths of Ca II H+K, Ba 4554 Å, and CN, CH and TiO.

The radial velocities confirm membership for nearly all stars, and display the known rotation of the cluster core. The metallicity distribution peaks around $[\text{Fe}/\text{H}] \sim -1.8$, with a secondary peak around $[\text{Fe}/\text{H}] \sim -0.8$.

The RR Lyrae stars pulsating in the 1st overtone are found to be warmer on average than those pulsating in the fundamental mode. Four stars pulsating with periods $P \gtrsim 1 \text{ d}$ have relatively low gravities, either because they have evolved towards the AGB and/or their masses are reduced as a result of mass loss. We tentatively identify a sample of low-amplitude variables in the blue part of the RR Lyrae instability strip on the basis of their relatively large variations in gravity between multiple measurements. For one RR Lyrae star we find blue-shifted hydrogen Balmer line emission.

Measurements of metallicities and temperatures purely on the basis of our spectroscopy do not always agree with the more commonly used methods in which the temperature is constrained with photometry; e.g., the anomalous RGB appears metal-poor in our data, contrary to what is generally accepted. This is likely the result of the inherent difficulty in modelling the atmospheres and spectra of cool stars, and the intrusion into the RGB-a optical colours and magnitudes regime by extreme AGB stars.

We identify several new cluster carbon stars, and find evidence for thermal pulses enriching M-type AGB stars with barium. This super-enhancement is distinct from the pre-enrichment in s-process elements by a previous generation of more massive AGB stars, which our measurements also confirm to have taken place.

We also identify several post-AGB stars and other UV-bright stars; their and the AGB star properties can be interpreted as mass loss on the RGB being slightly less efficient around $[\text{Fe}/\text{H}] \sim -2$ than around $[\text{Fe}/\text{H}] \sim -1$. Evidence for mass return into the ISM is present in the form of hydrogen line emission from post-AGB stars, and we postulate that some of the brightest carbon stars might eventually inject carbon-rich dust into the ISM.

Blue HB stars are used to probe the intervening ionized ISM in the Ca II H+K lines, revealing possible interaction between the cluster and surrounding diffuse matter. Higher-resolution spectra of more blue HB stars are required to confirm these results.

ACKNOWLEDGMENTS

We wish to thank Terry Bridges for performing the 2dF observations in his capacity as erstwhile 2dF fellow, and for his advice during the fibre configuration and data reduction stages. We are grateful to the referee whose insightful and constructive review helped clarify certain points in the manuscript. AS acknowledges the award of a Nuffield Foundation Undergraduate Research Bursary to perform part of this research. IMcD acknowledges an STFC studentship to fund his research on mass loss in globular clusters. This project was initiated while JvL was a PDRA at the IoA Cambridge, the hospitality of which is much appreciated.

REFERENCES

- Alonso A., Arribas A., Martínez-Roger C., 1999, *A&AS*, 140, 261
 Anderson A. J., 1997, PhD Thesis. University of California, Berkeley CA
 Bedin L. R., Piotto G., Anderson A. J., Cassisi S., King I. R., Momany Y., Carraro G., 2004, *ApJ*, 605, L125
 Behr B. B., Cohen J. G., McCarthy J. K., Djorgovski S. G., 1999, *ApJ*, 517, L135
 Bekki K., 2006, *MNRAS*, 367, L24
 Bland J. M., Altman D. G., 1996, *British Medical Journal*, 312, 1654
 Bond H. E., 1975, *ApJ*, 202, L47
 Boothroyd A. I., Sackmann I.-J., 1999, *ApJ*, 510, 232
 Boyer M. L., Woodward C. E., van Loon J. Th., Gordon K. D., Evans A., Gehrz R. D., Helton L. A., Polomski E. F., 2006, *AJ*, 132, 1415
 Boyer M. L., McDonald I., van Loon J. Th., Woodward C. E., Gehrz R. D., Evans A., Dupree A. K., 2007, *AJ*, submitted
 Buchler J. R., Kolláth Z., 2001, *ApJ*, 555, 961
 Butler D., Dickens R. J., Epps E., 1978, *ApJ*, 225, 148
 Caputo F., Degl'Innocenti S., Marconi M., 2002, in: *Omega Centauri: a unique window into astrophysics*, eds. F. van Leeuwen, J. Hughes & G. Piotto. ASP Conf.Ser. 265, p185
 Catelan M., 2005, in: *Resolved Stellar Populations*, eds. D. Valls-Gabaud & M. Chavez. ASP Conf.Ser. (arXiv:astro-ph/0507464)
 Clement C., 1997, Updated 3rd Catalogue of Variable Stars in Globular Clusters. VizieR On-line Data Catalog: V/97
 Cowley A. P., Crampton D., 1985, *PASP*, 97, 835
 D'Cruz N. L., Dorman B., Rood R. T., O'Connell R. W., 1996, *ApJ*, 466, 359
 Del Principe M., et al., 2006, *ApJ*, 652, 362
 Dickens R. J., 1972, *MNRAS*, 159, L7
 Drinkwater M. J. et al., 2004, *PASA*, 21, 375
 Dupree A. K., Smith G. H., 1995, *AJ*, 110, 405
 Ferraro F. R., Bellazzini M., Pancino E., 2002, *ApJ*, 573, L95
 Freeman K. C., 1993, in: *The globular clusters-galaxy connection*, eds. G.H. Smith & J.P. Brodie. ASP Conf.Ser. 48, p608
 Frogel J. A., Elias J. H., 1988, *ApJ*, 324, 823
 Gebhardt K., Rich R. M., Ho L. C., 2002, *ApJ*, 578, L41
 Gonzalez G., Wallerstein G., 1994, *AJ*, 108, 1325
 Greggio L., Renzini A., 1990, *ApJ*, 364, 35
 Harding G. A., 1962, *Observatory*, 82, 205
 Herwig F., 2005, *ARA&A*, 43, 435
 Hilker M., Richtler T., 2000, *A&A*, 362, 895
 Houdashelt M. L., Bell R. A., Sweigart A. V., Wing R. F., 2000a, *AJ*, 119, 1424
 Houdashelt M. L., Bell R. A., Sweigart A. V., 2000b, *AJ*, 119, 1448
 Jaschek C., Jaschek M., 1990, *The Classification of Stars*. Cambridge University Press, ISBN 0521389968
 Kayser A., Hilker M., Richtler T., Willemsen P. G., 2006, *A&A*, 458, 777
 Klypin A., Kravtsov A. V., Valenzuela O., Prada F., 1999, *ApJ*, 522, 82
 Kurucz R. L., 1993, Kurucz CD-ROM No.18. Smithsonian Astrophysical Observatory
 Kurucz R. L., 1999, Kurucz CD-ROM No.24. Smithsonian Astrophysical Observatory
 Landsman W. B., et al., 1992, *ApJ*, 395, L21
 Lee Y.-W., Joo J.-M., Sohn Y.-J., Rey S.-C., Lee H.-C., Walker A. R., 1999, *Nature*, 402, 55
 Lee Y.-W. et al., 2005, *ApJ*, 621, L57
 Lub J., 2002, in: *Omega Centauri: a unique window into astrophysics*, eds. F. van Leeuwen, J. Hughes & G. Piotto. ASP Conf.Ser. 265, p95
 McDonald I., van Loon J. Th., 2007, *A&A*, submitted
 Meylan G., Mayor M., 1986, *A&A*, 166, 122
 Meylan G., Mayor M., Duquenois A., Dubath P., 1995, *A&A*, 303, 761
 Merritt D., Meylan G., Mayor M., 1997, *AJ*, 114, 1074
 Norris J. E., 2004, *ApJ*, 612, L25
 Norris J. E., Freeman K. C., Mighell K. J., 1996, *ApJ*, 462, 241
 Norris J. E., Freeman K. C., Mayor M., Seitzer P., 1997, 487, L187
 Origlia L., Ferraro F. R., Bellazzini M., Pancino E., 2003, *ApJ*, 591, 916
 Pancino E., Ferraro F. R., Bellazzini M., Piotto G., Zoccali M., 2000, *ApJ*, 534, L83
 Pancino E., Pasquini L., Hill V., Ferraro F. R., Bellazzini M., 2002, *ApJ*, 568, L101
 Pancino E., Galfo A., Ferraro F. R., Bellazzini M., 2007, *ApJ*, 661, L155
 Pietrinferni A., Cassisi S., Salaris M., Castelli F., 2004, *ApJ*, 612, 168
 Piotto G. et al., 2005, *ApJ*, 621, 777
 Reijns R. A., Seitzer P., Arnold R., Freeman K. C., Ingerson T., van den Bosch R. C. E., van de Ven G., de Zeeuw P. T., 2006, *A&A*, 445, 503
 Renzini A., Fusi Pecci F., 1988, *ARA&A*, 26, 199
 Sandage A., Katem B., 1968, *ApJ*, 153, 569
 Sawyer Hogg H., 1973, *Publ. David Dunlap Obs., Univ. Toronto*, Vol. 3, No. 6
 Schröder K.-P., Cuntz M., 2005, *ApJ*, 630, L73
 Smith M. G., Wing R. F., 1973, *PASP*, 85, 659
 Smith V. V., Suntzeff N. B., Cunha K., Gallino R., Busso M., Lambert D. L., Straniero O., 2000, *AJ*, 119, 1239
 Sollima A., Ferraro F. R., Origlia L., Pancino E., Bellazzini M., 2004, *A&A*, 420, 173
 Sollima A., Pancino E., Ferraro F. R., Bellazzini M., Straniero O., Pasquini L., 2005, *ApJ*, 634, 332
 Sollima A., Borissova J., Catelan M., Smith H. A., Minniti D., Cacciari C., Ferraro F. R., 2006, *ApJ*, 640, L43
 Sollima A., Ferraro F. R., Bellazzini M., Origlia L., Straniero O., Pancino E., 2007, *ApJ*, 654, 915
 Stanford L. M., Da Costa G. S., Norris J. E., Cannon R. D., 2006a, *ApJ*, 647, 1075
 Stanford L. M., Da Costa G. S., Norris J. E., Cannon R. D., 2006b, *ApJ*, 653, L117
 Stanford L. M., Da Costa G. S., Norris J. E., 2007, *ApJ* in press (arXiv:0708.0096)
 Sweigart A. V., 1997, *ApJ*, 474, L23
 van de Ven G., van den Bosch R. C. E., Verolme E. K., de Zeeuw P. T., 2006, *A&A*, 445, 513
 van Leeuwen F., Le Poole R. S., Reijns R. A., Freeman K. C., de Zeeuw P. T., 2000, *A&A*, 360, 472
 van Leeuwen F., Le Poole R. S., 2002, in: *Omega Centauri: a unique window into astrophysics*, eds. F. van Leeuwen, J. Hughes & G. Piotto. ASP Conf.Ser. 265, p41

- van Loon J.Th., 2002, in: Omega Centauri: a unique window into astrophysics, eds. F. van Leeuwen, J. Hughes & G. Piotto. ASP Conf.Ser. 265, p129
- van Loon J.Th., 2006, in: Stellar Evolution at Low Metallicity: Mass Loss, Explosions, Cosmology, eds. H.J.G.L.M. Lamers, N. Langer, T. Nugis & K. Annuk. ASP Conf.Ser. 353, p211
- Villanova S. et al., 2007, ApJ, 663, 296
- Wasserburg G. J., Boothroyd A. I., Sackmann I.-J., 1995, ApJ, 447, L37
- Weldrake D. T. F., Sackett P. D., Bridges T. J., 2007, AJ, 133, 1447
- Wing R. F., Stock J., 1973, ApJ, 186, 979
- Woolley R. R., 1966, R.Obs.Ann., 2, 1
- Zinnecker H., Keable C. J., Dunlop J. S., Cannon R. D., Griffiths W. K., 1988, in: The Harlow Shapley Symposium on Globular Cluster Systems in Galaxies, eds. J.E. Grindlay & A.G. Davis Philip. IAUS 126 (Kluwer Academic Publishers), p603

APPENDIX A: MINIMISING DIFFERENTIAL TAYLOR SERIES EXPANSIONS IN PRACTICE

The observed spectrum, $f(x)$ is presumed to be described approximately as a Taylor series expanded to second order around each spectral point a ,

$$f(x) \simeq f(a) + (x - a) \left. \frac{df}{dx} \right|_{x=a} + \frac{(x - a)^2}{2!} \left. \frac{d^2f}{dx^2} \right|_{x=a}, \quad (\text{A1})$$

and the model spectrum, g , is written in identical fashion. Rather than striving to obtain $f(a) \equiv g(a)$, we search for the model which yields $f(x) \equiv g(x)$, in every point of the spectrum. Thus, with N spectral points we minimise the statistic

$$\chi^2 \equiv \sum_{i=1}^N (f_i(x) - g_i(x))^2. \quad (\text{A2})$$

In practice, we choose to evaluate the series expansion at a positive deviation by one spectral point, i.e. $(x - a_i) \equiv 1$. The 0th-order term is simply the difference between the model and observed spectrum at $x = a_i$,

$$\Delta_i = f_i(a_i) - g_i(a_i), \quad (\text{A3})$$

the 1st-order term corresponds to the slope around $x = a_i$,

$$\Delta'_i \simeq \frac{\Delta_{i+1} - \Delta_{i-1}}{2}, \quad (\text{A4})$$

whilst the 2nd-order term is estimated from the difference in slope at either side of $x = a_i$, i.e. in points a_{i+1} and a_{i-1} ,

$$\Delta''_i \simeq \frac{\Delta_{i+2} - \Delta_i}{2} - \frac{\Delta_i - \Delta_{i-2}}{2}. \quad (\text{A5})$$

Combination of Eqs. (A3-5) yields

$$\chi^2 \sim \sum_{i=1}^N \left(\frac{\Delta_{i+2} + \Delta_{i+1} - \Delta_{i-1} + \Delta_{i-2}}{2} \right)^2. \quad (\text{A6})$$

If the line core has a different slope from the model then it will increase the value of χ^2 ; if it is simply shallower then it will not contribute to χ^2 , but such discrepancies will, of course, contribute to χ^2 in adjacent points. A conspiracy could arise if Δ_{i+2} and Δ_{i-2} cancel each other and Δ_{i+1} and Δ_{i-1} are identical but not zero. Clearly the spectral shape around that point would be quite different in the model and

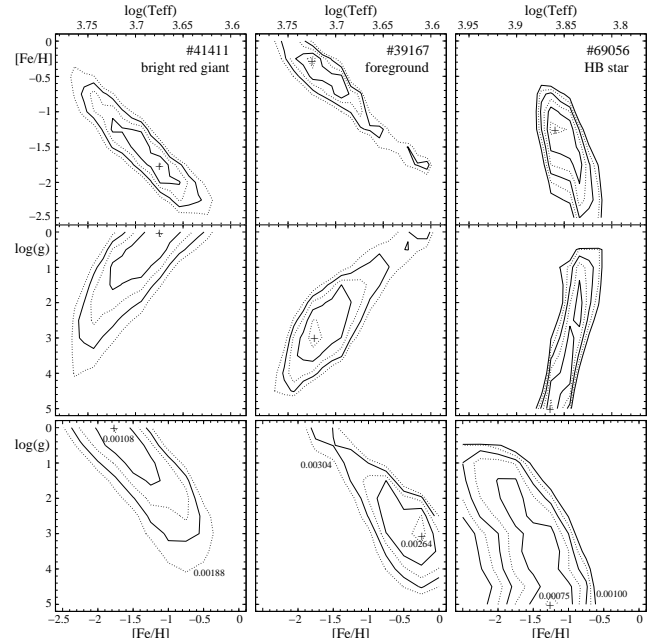


Figure A1. Maps of χ^2 , for the cluster red giant #41411 (left), foreground star #39167 (middle) and cluster HB star #69056 (right). Results are displayed for the best-matched velocity and combinations of two parameters $\in (T_{\text{eff}}, [\text{Fe}/\text{H}], \log(g))$ always wherever the third parameter reaches the minimum value for χ^2 . Lowest and highest contours are labelled; “+” marks minimum.

observed spectra, but although this might occur in individual spectral points the overall spectrum would be sufficiently different that it is highly unlikely to minimise χ^2 over the full spectrum.

Monte Carlo simulations were performed in which noise was added to a variety of spectra produced from the ATLAS9 models. The method recovered the input, never deviating by more than one step as long as the S/N ratio exceeded ~ 10 . The model spectra are highly idealised versions, though, and in reality stellar spectra deviate for many reasons. The traditional χ^2 method on a pixel-by-pixel basis is susceptible to single, strong spectral features such as the CN bands or Ca H+K lines. These were sometimes noticed to drive the solution into an extreme corner of parameterspace whereas our modified χ^2 method would find a more “expected” solution (e.g., $[\text{Fe}/\text{H}] \sim -1.75$, or low gravity in case of a bright cluster red giant or high gravity in case of an extreme HB star, et cetera). Our method thus seems more robust than the traditional χ^2 minimisation, as it takes account of correlated behaviour due to spectral structure.

To illustrate the contrast of χ^2 in parameterspace, χ^2 maps are shown in Fig. A1 for three cases, always for the best-matched velocity. In each map, for each pair of values of the two parameters on the axes the minimum value of χ^2 is plotted, i.e. it is not a simple cross-section through the $(T_{\text{eff}}, [\text{Fe}/\text{H}], \log(g))$ parameterspace but a projection of where χ^2 is minimal. This more accurately maps the space where solutions tend to migrate, but it means that the corresponding value of the third parameter varies across each map. Cooler solutions tend to be accompanied by lower metallicity to offset the diminished line opacity. The method easily distinguishes between a metal-poor cluster red giant

(Fig. A1, left panels) and a metal-rich foreground star (Fig. A1, middle panels). The gravity for HB stars (Fig. A1, right panels) is less well constrained though this hardly affects the solution for T_{eff} and to a lesser extent $[\text{Fe}/\text{H}]$.